



IMPLEMENTING MULTI-SCALE AGRICULTURAL INDICATORS EXPLOITING SENTINELS

**VEGETATION FIELD DATA AND PRODUCTION OF GROUND-
BASED MAPS:**

**“ALBUFERA SITE, VALENCIA, SPAIN”
JUNE - AUGUST 2014**

ISSUE I1.10

EC Proposal Reference N° FP7-311766

Actual submission date : January 2015

Start date of project: 01.06.2014

Duration : 40 months

Name of lead partner for this deliverable: EOLAB

Book Captain: Vicent Sendra (EOLAB)

Contributing Authors: Consuelo Latorre (EOLAB), Fernando Camacho (EOLAB), Jorge Sánchez (EOLAB), Javier García Haro (Universitat de València), Manuel Campos-Taberner (Universitat de València), Beatriz Martínez (Universitat de València).

Project co-funded by the European Commission within the Seventh Framework Program (2007-2013)		
Dissemination Level		
PU	Public	X
PP	Restricted to other programme participants (including the Commission Services)	
RE	Restricted to a group specified by the consortium (including the Commission Services)	
CO	Confidential, only for members of the consortium (including the Commission Services)	

DOCUMENT RELEASE SHEET

Book Captain:	Vicent Sendra	Date: 08.06.2016	Sign. 
Approval:	R. Lacaze	Date: 10.06.2016	Sign. 
Endorsement:	M. Koleva	Date:	Sign.
Distribution:	Public		

CHANGE RECORD

Issue/Revision	Date	Page(s)	Description of Change	Release
I1.00	20.01.2015	All	First issue	I1.00
I1.10	08.06.2016	44, 46, 48	Update RMSE for fifth campaign	I1.10

TABLE OF CONTENTS

1. Background of the Document	12
1.1. Executive Summary	12
1.2. Portfolio	12
1.3. Scope and Objectives	13
1.4. Content of the Document	13
2. Introduction.....	15
3. Study area	17
3.1. Location.....	17
3.2. Description of The Test Site	17
4. Ground measurements	19
4.1. Material and Methods	19
4.1.1. Digital Hemispheric Photographs (DHP)	20
4.1.2. AccuPARLP80-Ceptometer.....	22
4.1.3. LI-COR LAI-2000 and LI-COR LAI-2200C plant canopy analyser	23
4.1.4. Mobile app: PocketLAI	25
4.2. Spatial Sampling Scheme	25
4.3. ground data.....	27
4.3.1. Data processing.....	27
4.3.2. Inter-comparison of different instruments.....	28
4.3.3. Content of the Ground Dataset	33
5. Evaluation of the sampling	37
5.1. Principles.....	37
5.2. Evaluation Based On NDVI Values.....	37
5.3. Evaluation Based On Convex Hull: Product Quality Flag.	39
6. production of ground-based maps.....	41
6.1. Imagery	41
6.2. The Transfer Function	42
6.2.1. The regression method.....	42
6.2.2. Band combination.....	42
6.2.3. The selected Transfer Function.....	46
6.3. The High Resolution Ground Based Maps	50
6.3.1. Mean values for validation	53

7. Conclusions.....	55
8. Acknowledgements	57
9. References.....	58

LIST OF FIGURES

Figure 1: People involved in the Field Campaign. La Albufera site (Spain), 2014.	16
Figure 2: Location of La Albufera site near Valencia (Spain)	17
Figure 3: The lagoon and typical rice fields in La Albufera Site.	18
Figure 4: AccuPAR LP80-Ceptometer	23
Figure 5: LAI-2000 device (left) and LAI-2200C device (right).....	24
Figure 6: LAI-2200 optical sensor with 5 zenith angles.....	25
Figure 7: Distribution of the sampling units (ESU) over the study area. La Albufera site (Spain), 2014.....	26
Figure 8: Example of the CAN-EYE processing carried out on rice ESU. a) DHP images. b) Classified images. c) Average gap fraction. d) Clumping factor versus view zenith angle.	27
Figure 9: DHP picture and the result of the CAN-EYE processing for dense rice sample unit (ESU L6). La Albufera site (Spain), 2014.	28
Figure 10: Mean LAI _{eff} values derived using AccuPAR LP80, mobile APP, DHPs, LAI-2000 and LAI-2200 during the field campaign for 3 ESUs (L1, L5 and L10). La Albufera site (Spain), 2014.	29
Figure 11: Mean FAPAR values derived using AccuPAR LP-80, DHP-C and DHP-N during the field campaign for 3 ESUs (L1, L5 and L10). La Albufera site (Spain), 2014.....	30
Figure 12: Scatter plots of LAI _{eff} values measured with different devices. a) DHP-C vs DHP-N. b) DHP-C vs LAI2000. a) DHP-C vs LP-80. d) DHP-C vs APP. La Albufera site (Spain), 2014.....	30
Figure 13: Scatter plots of LAI measured with 2 different DHP devices. La Albufera site (Spain), 2014....	31
Figure 14: Scatter plots of FAPAR measured with different devices. a) DHP-C vs LP-80. b) DHP-C vs DHP-N. c) DHP-N vs LP-80. La Albufera site (Spain), 2014.	31
Figure 15: Scatter plots of F _{cover} measured values with DHP-C and DHP-N. La Albufera site (Spain), 2014.....	32
Figure 16: Scatter plots of LAI _{eff} for 3 instruments: a) DHP-N vs LAI-2000, b) LAI-2000 vs APP, c) DHP-N vs APP. Albufera Site (Spain), 2014.....	32
Figure 17: Mean values and standard deviation: a) LAI _{eff} and LAI. b) FAPAR at 10:00. c) F _{cover} . Albufera site (Spain), 2014.	34
Figure 18: Histograms of LAI _{eff} ground data measurements for different campaigns. Albufera site (Spain), 2014.....	35
Figure 19: Histograms of FAPAR at 10:00 a.m. and F _{cover} ground data measurements for different campaigns. Albufera site (Spain), 2014.	36
Figure 20: Comparison of NDVI (TOA) distribution between ESUs (green dots) and over the whole image (Blue line). Albufera site (Spain), 2014.	38
Figure 21: Convex Hull test over 20x20km ² area centered at the test site: clear and dark blue correspond to the pixels belonging to the 'strict' and 'large' convex hulls, red corresponds to the pixels for which the transfer function is extrapolating and black pixels represent water bodies. Yellow square marks the 5x5km ² study area. Albufera site (Spain), 2014.....	40
Figure 22: Test of multiple regressions (Transfer Function) applied on different band combinations. Band combinations are given in abscissa (1=G, 2=RED, 3=NIR and 4=SWIR). The weighted root mean square error (RW) is presented in red along with the cross-validation RMSE (RC) in green. First Campaign (2014.06.17), Albufera site (Spain), 2014.	43
Figure 23: Test of multiple regressions (Transfer Function) applied on different band combinations. Band combinations are given in abscissa (1=G, 2=RED, 3=NIR and 4=SWIR). The weighted root mean square	

error (RW) is presented in red along with the cross-validation RMSE (RC) in green. Second Campaign (2014.06.24), Albufera site (Spain), 2014. 44

Figure 24: Test of multiple regressions (Transfer Function) applied on different band combinations. Band combinations are given in abscissa (1=G, 2=RED, 3=NIR and 4=SWIR). The weighted root mean square error (RW) is presented in red along with the cross-validation RMSE (RC) in green. Fifth Campaign (2014.07.17), Albufera site (Spain), 2014. 44

Figure 25: Test of multiple regressions (Transfer Function) applied on different band combinations. Band combinations are given in abscissa (1=G, 2=RED, 3=NIR and 4=SWIR). The weighted root mean square error (RW) is presented in red along with the cross-validation RMSE (RC) in green. Eighth Campaign (2014.08.07), Albufera site (Spain), 2014. 45

Figure 26: Test of multiple regressions (Transfer Function) applied on different band combinations. Band combinations are given in abscissa (1=G, 2=RED, 3=NIR and 4=SWIR). The weighted root mean square error (RW) is presented in red along with the cross-validation RMSE (RC) in green. Ninth Campaign (2014.08.22), Albufera site (Spain), 2014. 45

Figure 27: LAleff, LAI, FAPAR 10 a.m. and FCover results for regression on reflectance using 4 bands combination. First Campaign (2014.06.17), Albufera site (Spain), 2014. 47

Figure 28: LAleff, LAI, FAPAR 10 a.m. and FCover results for regression on reflectance using 4 bands combination. Second Campaign (2014.06.24), Albufera site (Spain), 2014. 48

Figure 29: LAleff, LAI, FAPAR 10 a.m. and FCover results for regression on reflectance using 4 bands combination. Fifth Campaign (2014.07.15), Albufera site (Spain), 2014. 48

Figure 30: LAleff, LAI, FAPAR 10 a.m. and FCover results for regression on reflectance using 4 bands combination. Eighth Campaign (2014.08.07), Albufera site (Spain), 2014. 49

Figure 31: LAleff, LAI, FAPAR 10 a.m. and FCover results for regression on reflectance using 4 bands combination. Ninth Campaign (2014.08.22), Albufera site (Spain), 2014. 49

Figure 32: Ground-based LAleff maps (20x20 km²) retrieved on the Albufera Site for each campaign. Red square marks the 5x5 study area. 50

Figure 33: Ground-based LAI maps (20x20 km²) retrieved on the Albufera Site for each campaign. Red square marks the 5x5 study area. 51

Figure 34: Ground-based FAPAR at 10:00 maps (20x20 km²) retrieved on the Albufera Site for each campaign. Red square marks the 5x5 study area. 52

Figure 35: Ground-based FCover maps (20x20 km²) retrieved on the Albufera Site for each campaign. Red square marks the 5x5 study area. 53

LIST OF TABLES

<i>Table 1: Coordinates and altitude of the test site.</i>	<i>17</i>
<i>Table 2: Biophysical variables measured per campaign and transfer function realized.</i>	<i>19</i>
<i>Table 3: Instruments used by each group.....</i>	<i>19</i>
<i>Table 4: Instruments used and total number of ESU's per campaign.....</i>	<i>26</i>
<i>Table 5: Header used to describe ESUs with the ground measurements.</i>	<i>33</i>
<i>Table 6: Number of ESUs per campaign.</i>	<i>37</i>
<i>Table 7: Landsat-8 cloud-free images available.</i>	<i>41</i>
<i>Table 8: Characteristics of Landsat-8 input data imagery.....</i>	<i>42</i>
<i>Table 9: Transfer function applied to the whole site for LAI_{eff}, LAI, FAPAR 10:00 a.m. and FCover for campaigns of 17th June, 24th June, 15th July and 7th August and 22nd August 2014. RW stands for weighted RMSE, and RC stands for cross-validation RMSE.</i>	<i>46</i>
<i>Table 10: Transfer function applied to the whole site for LAI_{eff}, LAI, FAPAR 10:00 a.m. and FCover for campaign of 22nd August 2014. RW stands for weighted RMSE, and RC stands for cross-validation RMSE.</i>	<i>47</i>
<i>Table 11: Mean values and standard deviation (STD) of the HR biophysical maps for the selected 3x3 km² areas at Albufera site.</i>	<i>54</i>
<i>Table 12: Content of the dataset.....</i>	<i>54</i>

LIST OF ACRONYMS

CEOS	Committee on Earth Observation Satellite
CEOS LPV	Land Product Validation Subgroup
CEOS OLIVE	On Line Interactive Validation Exercise Subgroup
DG AGRI	Directorate General for Agriculture and Rural Development
DG RELEX	Directorate General for External Relations (European Commission)
DHP	Digital Hemispheric Photographs
EO	Earth Observation
ERMES	Earth Observation Model Based on Rice Information Service
ESA	European Space Agency
ESU	Elementary Sample Unit
EUROSTATS	Directorate General of the European Commission
FAPAR	Fraction of Absorbed Photo-synthetically Active Radiation
FAO	Food and Agriculture Organization
FCOVER	Fraction of Vegetation Cover
FIPAR	Fraction of Intercepted Photosynthetically
FP7	Seventh Framework Program
GCP	Ground Control Point
GEOGLAM	Global Agricultural Geo- Monitoring Initiative
GMES	Global Monitoring for Environment and Security
IMAGINES	Implementing Multi-scale Agricultural Indicators Exploiting Sentinels
JECAM	Joint Experiment for Crop Assessment and Monitoring
LAI	Leaf Area Index
LDAS	Land Data Assimilation System
LRS	Local Rice Service
LUT	Look-up-table techniques
MSG	Meteosat Second Generation
NDVI	Normalized Difference Vegetation Index
NIR	Near Infrared
PAI	Plant Area Index
PAR	Photosynthetically Active Radiation.
PROBA-V	Project for On-Board Autonomy satellite, the V standing for vegetation.
RMSE	Root Mean Square Error
RRS	Regional Rice Service
SPOT /VGT	Satellite Pour l'Observation de la Terre / VEGETATION
SWIR	Short Wave Infrared
TOA	Top of Atmosphere Reflectance

UTM	Universal Transverse Mercator coordinates system
UV	Universitat de València
VALERI	Validation of Land European Remote sensing Instruments
WGS-84	World Geodetic System

1. BACKGROUND OF THE DOCUMENT

1.1. EXECUTIVE SUMMARY

The Copernicus Land Service has been built in the framework of the FP7 geoland2 project, which has set up pre-operational infrastructures. IMAGINES intends to ensure the continuity of the innovation and development activities of geoland2 to support the operations of the global land component of the GMES Initial Operation (GIO) phase. In particular, the use of the future Sentinel data in an operational context will be prepared. Moreover, IMAGINES will favor the emergence of new downstream activities dedicated to the monitoring of crop and fodder production.

The main objectives of IMAGINES are to (i) improve the retrieval of basic biophysical variables, mainly LAI, FAPAR and the surface albedo, identified as Terrestrial Essential Climate Variables, by merging the information coming from different sensors (PROBA-V and Landsat-8) in view to prepare the use of Sentinel missions data; (ii) develop qualified software able to process multi-sensor data at the global scale on a fully automatic basis; (iii) complement and contribute to the existing or future agricultural services by providing new data streams relying upon an original method to assess the above-ground biomass, based on the assimilation of satellite products in a Land Data Assimilation System (LDAS) in order to monitor the crop/fodder biomass production together with the carbon and water fluxes;(iv) demonstrate the added value of this contribution for a community of users acting at global, European, national, and regional scales.

Further, IMAGINES serves the growing needs of international (e.g. FAO and NGOs), European (e.g. DG AGRI, EUROSTATS, DG RELEX), and national users (e.g. national services in agro-meteorology, ministries, group of producers, traders) on accurate and reliable information for the implementation of the EU Common Agricultural Policy, of the food security policy, for early warning systems, and trading issues. IMAGINES will also contribute to the Global Agricultural Geo-Monitoring Initiative (GEO-GLAM) by its original agriculture service which can monitor crop and fodder production together with the carbon and water fluxes and can provide drought indicators, and through links with JECAM (Joint Experiment for Crop Assessment and Monitoring).

1.2. PORTFOLIO

The IMAGINESS portfolio contains global and regional biophysical variables derived from multi-sensor satellite data, at different spatial resolutions, together with agricultural indicators, including the above-ground biomass, the carbon and water fluxes, and drought indices resulting from the assimilation of the biophysical variables in the Land Data Assimilation System (LDAS).

The production in Near Real Time of the 333m resolution products, at a frequency of 10 days, using PROBA-V data is carried out in the Copernicus Global Land Service (<http://land.copernicus.eu/global/>).

The demonstration of high resolution (30m) products derived from Landsat-8 was done over demonstration sites of cropland and grassland in contrasting climatic and environmental conditions. Demonstration products are available on the ImagineS website (<http://www.fp7-imagines.eu/pages/services-and-products/landsat-8-biophysical-products.php>)

1.3. SCOPE AND OBJECTIVES

The main objective of this document is to describe the field campaign and ground data collected at Albufera site in Valencia, Spain, and the up-scaling of the ground data to produce ground-based high resolution maps of the following biophysical variable:

- Leaf Area Index (LAI), defined as half of the total developed area of leaves per unit ground surface area (m^2/m^2). We focused on two different LAI quantities (for green elements):
 - The effective LAI (LAI_{eff}) derived from the description of the gap fraction as a function of the view zenith angle. In addition, effective LAI measures derived at 57.5° are also provided in the ground database.
 - The actual LAI (LAI) accounting for the clumping index.
- Fraction of green Vegetation Cover (FCover), defined as the proportion of soil covered by vegetation, derived from the gap fraction between 0° and 10° of view zenith angle.
- Fraction of Absorbed Photosynthetically Active Radiation (FAPAR), which is the fraction of the photosynthetically active radiation (PAR) absorbed by a vegetation canopy. PAR is the solar radiation reaching the canopy in the 0.4–0.7 μm wavelength region. We focused on the instantaneous ‘black-sky’ FAPAR at 10:00 a.m. which is the FAPAR under direct illumination conditions at a given solar position. In addition, two other quantities are provided: daily integrated FAPAR, computed as the black-sky FAPAR integrated over the day, and the ‘white-sky’ FAPAR, which is the FAPAR under diffuse illumination conditions.

1.4. CONTENT OF THE DOCUMENT

This document is structured as follows:

- Chapter 2 provides an introduction to the field experiment.
- Chapter 3 provides the location and description of the site.
- Chapter 4 describes the ground measurements, including material and methods, sampling and data processing.

- Chapter 5 provides an evaluation of the sampling.
- Chapter 6 describes the production of high resolution ground-based maps, and the selected “mean” values for validation.

2. INTRODUCTION

Validation of remote sensing products is mandatory to guaranty that the satellite products meets the user's requirements. Protocols for validation of global LAI products are already developed in the context of Land Product Validation (LPV) group of the Committee on Earth Observation Satellite (CEOS) for the validation of satellite-derived land products (Fernandes et al., 2014), and recently applied to Copernicus global land products based on SPOT/VGT observation (Camacho et al., 2013). This generic approach is made of 2 major components:

- The indirect validation: including inter-comparison between products as well as evaluation of their temporal and spatial consistency
- The direct validation: comparing satellite products to ground measurements of the corresponding biophysical variables. In the case of low and medium resolution sensors, the main difficulty relies on scaling local ground measurements to the extent corresponding to pixels size. However, the direct validation is limited by the small number of sites, for that reason a main objective of IMAGINES is the collection of ground truth data in demonstration sites.

The content of this document is compliant with existing validation guidelines (for direct validation) as proposed by the CEOS LPV group (Morissette et al., 2006); the VALERI project (<http://w3.avignon.inra.fr/valeri/>) and ESA campaigns (Baret and Fernandes, 2012). It therefore follows the general strategy based on a bottom up approach: it starts from the scale of the individual measurements that are aggregated over an elementary sampling unit (ESU) corresponding to a support area consistent with that of the high resolution imagery used for the up-scaling of ground data. Several ESUs are sampled over the site. Radiometric values over a decametric image are also extracted over the ESUs. This will be later used to develop empirical transfer functions for up-scaling the ESU ground measurements (e.g. Martínez et al., 2009). Finally, the high resolution ground based map will be compared with the medium resolution satellite product at the spatial support of the product.

On the other hand, the FP7 ERMES project (<http://www.ermes-fp7space.eu/>) aims to develop a prototype of downstream services based on the assimilation of EO and in situ data within crop model. Two services are foreseen: 1) Regional Rice Service (RRS) customised for providing public authorities with an agro-monitoring system for crop mapping, yield estimating and risk forecast; 2) Local Rice Service (LRS) for the private sector (farmers, agro-services) providing added value information on yield variability, risk alert and crop damage at farm scale. La Albufera of Valencia, (Spain), is one of the pilot areas of the ERMES project, and one of the demonstration sites of IMAGINES where PROBA-V 333 LAI product will be assimilated into the agro-monitoring ERMES system.

A join multi-temporal field campaign to characterize the vegetation biophysical variables at La Albufera test site was carried out by the UV (Universitat de València), involved in ERMES project and EOLAB (involved in ImagineS). The field campaign was conducted from mid-June to end of August of 2014.

Multi-temporal Field Campaign: June - August 2014.

Teams involved in field collection:

Universitat de València: Javier García-Haro, Manuel Campos-Taberner, Beatriz Martínez.

EOLAB: Consuelo Latorre, Fernando Camacho, Jorge Sánchez, Vicent Sendra

Contact:

EOLAB: Fernando Camacho (fernando.camacho@eolab.es)

Universitat de València : Javier García-Haro (J.Garcia.Haro@uv.es)



Figure 1: People involved in the Field Campaign. La Albufera site (Spain), 2014.

3. STUDY AREA

3.1. LOCATION

The experimental site is located in La Albufera Natural Park, only 10 km from Valencia City, in the east coast of Spain, near Mediterranean Sea. The central coordinate of the study area is 39.274369° N, -0.316439° E (Figure 2).



Figure 2: Location of La Albufera site near Valencia (Spain).

Table 1: Coordinates and altitude of the test site.

20x20 km ² Center Site	
Geographic Lat/lon, WGS-84 (degrees)	Latitude = 39.274369° N Longitude = -0.316439° E
Altitude:	0 m

3.2. DESCRIPTION OF THE TEST SITE

The study zone has a subtropical Mediterranean climate, with very mild winters and long warm to hot summers with high humidity. Its average annual temperature is 17.8 °C. In the coldest month — January, the average temperature is 11.5 ° C and in the warmest month — August, is 25.5° C. The average annual precipitation is 454 mm, usually gathered in autumn.

La Albufera of Valencia is Natural Park and protected wetland area. It has a rich variety of flora and fauna, especially for its bird fauna and because here live 2 endemic Valencian little fishes *Alphanius iberus* and *Valencia hispanica*.

It is peculiar wetland where 3 different zones can be identified:

A **sandbar**, it separates the lagoon from the sea. Here there are beaches with dunes and a typical Mediterranean forest.

A freshwater **lagoon**, with an extension of 2.837 ha is the biggest lagoon of Spain. The average depth is only 80 cm with maximums of 2 m.

A **marsh**, in the past it was part of the lagoon but now is dedicated to rice crops with all the irrigation system (Figure 3).

The park is famous for the growing of rice; it has created the iconography of the place since the 18th century. The rice dishes belong to the Valencian culture, and the worldwide known 'Paella' was originated in La Albufera.



Figure 3: The lagoon and typical rice fields in La Albufera Site.

4. GROUND MEASUREMENTS

Ground data measurements were acquired through 9 field campaigns realized between 17th of June and 22th of August. All the field campaigns have LAI_{eff} measurements, whereas LAI, FAPAR 10 a.m. and FCover were collected in 5 field campaigns (Table 2).

Table 2: Biophysical variables measured per campaign and transfer function realized.

CAMPAIGN	DATE	LAI _{eff}	LAI	FAPAR	FCover	TRANSFER FUNCTION
1 st (C1)	2014.06.17	✓	✓	✓	✓	✓
2 nd (C2)	2014.06.24	✓	✓	✓	✓	✓
3 rd (C3)	2014.06.29	✓	X	X	X	X
4 th (C4)	2014.07.06	✓	X	X	X	X
5 th (C5)	2014.07.15	✓	✓	✓	✓	✓
6 th (C6)	2017.07.22	✓	X	X	X	X
7 th (C7)	2014.07.31	✓	X	X	X	X
8 th (C8)	2014.08.07	✓	✓	✓	✓	✓
9 th (C9)	2014.08.22	✓	✓	✓	✓	✓



Measured data



Missing data

The ground measurement database reported here was acquired by 2 groups, *Universitat de València* and *EOLAB*. Each group have used different instruments, table 3 summarizes it.

Table 3: Instruments used by each group.

	INSTRUMENTS
EOLAB	DHP (Canon), ACCUPAR LP-80, LAI-2200
Universitat de València	DHP (Nikon), LAI-2000, PocketLAI mobile App

4.1. MATERIAL AND METHODS

Several devices were used for estimating biophysical variables in the study area, including hemispherical digital photography (DHP), ceptometers, LI-COR LAI 2000 and

LI-COR LAI 2200C plant canopy analyser and also a Mobile application (PocketLAI App).

4.1.1. Digital Hemispheric Photographs (DHP)

DHP were acquired with a digital camera. Hemispherical photos allow the calculation of LAI, FAPAR and FCover measuring gap fraction through an extreme wide-angle camera lens (i.e. 180°) (Weiss et al., 2004). It produces circular images that record the size, shape, and location of gaps, either looking upward from within a canopy or looking downward from above the canopy. Each one of the 2 teams involved in the field campaigns used their own camera, so there are measurements from 2 different cameras.

EOLAB (DHP-C): *CANON EOS 6D and a SIGMA 8mm F3.5 – EX DG.*

Universitat de València (DHP-N): *NIKON COOLPIX 5000 with FC-E8 fisheye converter.*

The hemispherical photos acquired during the field campaign were processed with the CAN-EYE software (developed by INRA <http://www6.paca.inra.fr/can-eye>) to derive LAI, FAPAR and FCover. It is based on a RGB colour classification of the image to discriminate vegetation elements from background (i.e., gaps). This approach allows exploiting downward-looking photographs for short canopies (background = soil) as well as upward-looking photographs for tall canopies (background = sky). CAN-EYE software processes simultaneously up to 20 images acquired over the same ESU. Note that our images were acquired with similar illumination conditions to limit the variation of colour dynamics between images.

The processing is achieved in 3 main steps (Weiss et al., 2004). First, image pre-processing is performed, which includes removing undesired objects (e.g. operator, sun glint) and image contrast adjustments to ensure a better visual discrimination between vegetation elements and background. Second, an automatic classification (k-means clustering) is applied to reduce the total number of distinctive colours of the image to 324 which is sufficient to ensure accurate discrimination capacities while keeping a small enough number of colours to be easily manipulated. Finally, a default classification based on predefined colour segmentation is first proposed and then iteratively refined by the user. The allocation of the colours to each class (vegetation elements versus background) is the most critical phase that needs to be interactive because colours depend both on illumination conditions and on canopy elements. At the end of this process a binary image, background versus vegetation elements (including both green and non-green elements) is obtained.

The CAN-EYE software computes biophysical variables from gap fraction as follows:

Effective LAI (LAI_{eff}): Among the several methods described in Weiss et al (2004), the LAI estimation in the CAN-EYE software is performed by model inversion.

The LAI is estimated from the Plant Area Index (PAI) which is the variable estimated by CAN-EYE, as no distinction between leaves or other plant elements are made from the gap fraction estimates. PAI is very close to LAI for croplands or shrublands when pictures are taken downward looking, whereas larger discrepancies are expected in forest when pictures are taken upward looking. LAI are directly retrieved by inverting Eq. (1) (Poisson model) and assuming an ellipsoidal distribution of the leaf inclination using look-up-table (LUT) techniques.

$$P_0(\theta_v, \varphi_v) = e^{-N \cdot (\theta_v, \varphi_v)} = e^{-G \cdot (\theta_v, \varphi_v) \cdot \frac{LAI}{\cos(\theta_v)}} \quad \text{Eq. (1)}$$

A large range of random combinations of LAI (between 0 and 10, step of 0.01) and ALA (Average Leaf Angle) (10° and 80°, step of 2°) values is used to build a database made of the corresponding gap fraction values (Eq.1) in the zenithal directions defined by the CAN-EYE user (60° for the DHP collection in this field campaign). The process consists then in selecting the LUT element in the database that is the closest to the measured P_0 . The distance (cost function C_k) of the k^{th} element of the LUT to the measured gap fraction is computed as the sum of two terms. The first term computes a weighted relative root mean square error between the measured gap fraction and the LUT one. The second term is the regularization term that imposes constraints to improve the PAI estimates. Two equations are proposed for the second “regularization” term:

(1) constraint used in CAN-EYE V5.1 on the retrieved ALA values that assume an average leaf angle close to $60^\circ \pm 03^\circ$, and

(2) constraint used in CAN-EYE V6.1 on the retrieved PAI value that must be close from the one retrieved from the zenithal ring at 57° . This constraint is more efficient, but it can be computed only when the 57° ring is available (i.e., $COI \geq 60^\circ$)

The software also proposed other ways of computing PAI and ALA effective using Miller’s formula (Miller, 1967) which assumed that gap fraction only depends from view zenith angle. Furthermore, the CAN-EYE makes an estimation using the Welles and Norman (1991) method used in LAI-2000 for 5 rings. These LAI2000-like estimates were not used here as are based on the same Miller’s formula but using limited angular sampling.

LAI: The actual LAI that can be measured only with a planimeter with however possible allometric relationships to reduce the sampling, is related to the effective leaf area index through:

$$LAI_{eff} = \lambda_0 \cdot LAI \quad \text{Eq. (2)}$$

Where λ_0 is the clumping index. In CAN-EYE, the clumping index is computed using the Lang and Xiang (1986) logarithm gap fraction averaging method, although some uncertainties are associated to this method (Demarez et al., 2008). The principle is

based on the assumption that vegetation elements are locally assumed randomly distributed. Values of clumping index given by CAN_EYE are in certain cases correlated with the size of the cells used to divide photographs.

As the CAN-EYE software provides different results (CEV6.1, CEV5.1 and Miller's) for LAI and LAI_{eff} variables; an average LAI value was provided as ground estimate, and the standard deviation of the different method LAI estimates was reported as the uncertainty of the estimate.

FCover is retrieved from gap fraction between 0 to 10°.

$$FCOVER = 1 - P_0 \cdot (0 - 10^\circ) \quad \text{Eq. (3)}$$

FAPAR: As there is little scattering by leaves in that particular spectral domain due to the strong absorbing features of the photosynthetic pigments, FAPAR is often assumed to be equal to FIPAR (Fraction of Intercepted Photosynthetically Active Radiation), and therefore to the gap fraction. The actual FAPAR is the sum of two terms, weighted by the diffuse fraction in the PAR domain: the 'black sky' FAPAR that corresponds to the direct component and the 'white sky' or the diffuse component.

The instantaneous "Black-sky FAPAR" (FAPAR^{BS}) is given at a solar position (date, hour and latitude). Depending on latitude, the CAN EYE software computes the solar zenith angle every solar hour during half the day (there is symmetry at 12:00). The instantaneous FAPAR is then approximated at each solar hour as the gap fraction in the corresponding solar zenith angle:

$$FAPAR^{BS}(\theta_S) = 1 - P_0 \cdot (\theta_S) \quad \text{Eq. (4)}$$

The daily integrated black sky or direct FAPAR is computed as the following:

$$FAPAR_{Day}^{BS} = \frac{\int_{sunset}^{sunrise} \cos(\theta_S) \cdot [1 - P_0 \cdot (\theta_S)] \cdot d\theta}{\int_{sunset}^{sunrise} \cos(\theta_S) \cdot d\theta} \quad \text{Eq. (5)}$$

4.1.2. AccuPARLP80-Ceptometer

The AccuPAR model LP-80 (Figure 4) is a lightweight, portable, linear Photosynthetically Active Radiation (PAR) sensor. It lets you measure canopy PAR interception and calculate leaf area index (LAI) at any location within a plant or forest canopy. PAR data can be used with other climate data to estimate biomass production without destroying the crop. PAR is also important in determining other canopy processes; such as radiation interception, energy conversion, momentum, gas exchange, precipitation interception, and evapotranspiration.

It consists of an integrated microprocessor-driven data logger and probe. The probe contains 80 independent sensors, spaced 1 cm apart. The photo sensors measure PAR in the 400 to 700 nm waveband. The AccuPAR displays PAR in units of micro-mols per meter squared per second ($\mu\text{mol} \times \text{m}^{-2} \times \text{s}^{-1}$). The instrument is capable of hand-held or unattended measurement.



Figure 4: AccuPAR LP80-Ceptometer

For AccuPAR, the effective PAI is derived following the equations to predict the scattered and transmitted PAR (Norman and Welles, 1983).

$$PAI_{eff} = \frac{\left[\left(1 - \frac{1}{2k}\right) f_b^{-1} - 1 \right] \ln \tau}{A(1 - 0.47 f_b)} \quad \text{Eq.(6)}$$

Where τ is the transmission coefficient obtained through the ratio of the below canopy and the above canopy PARs, f_b is the fraction of incident beam PAR, A is a function of the leaf absorptivity (a) in the PAR band (AccuPAR assumes $a = 0.9$, and $A=0.86$ in LAI sampling routines), and k is the extinction coefficient for the canopy. We used $k=1$ for rice crops.

4.1.3. LI-COR LAI-2000 and LI-COR LAI-2200C plant canopy analyser

The LAI-2000 (LI-COR Inc., Lincoln, Nebraska, 2009) and LAI-2200C (LI-COR Inc., Lincoln, Nebraska, 2013) are the 2 models of plant canopy analyser used in the field campaigns. The *Universitat de València* team used the LI-COR LAI-2000 device whereas *EOLAB* team used the LI-COR LAI-2200C device. If the measurements are done correctly, both instruments must give the same results. The new features of the LAI-2200C device respect LAI-2000 device are USB connection, increased memory, lighter weight ergonomic design and a new menu driven software (Figure 5).

These instruments calculate Leaf Area Index (LAI) and other canopy attributes from light measurements made with a “fish-eye” optical sensor (148° field-of-view). Measurements made above and below the canopy are used to calculate canopy light

interception at five zenith angles (Figure 6). The average probability of light penetration into the canopy is computed by

$$\overline{P(\theta_i)} = \frac{1}{N_{obs}} \sum_{j=1}^{N_{obs}} \frac{B_{ij}}{A_{ij}} \quad \text{Eq. (7)}$$

where the subscript i ($i = 1 \dots 5$) refers to the optical sensor rings centered at θ_i and j refers to the number of observational pairs ($j = 1 \dots N_{obs}$). B_{ij} and A_{ij} are the j^{th} below and above canopy readings, respectively, for the i^{th} ring. The gap fraction for the i^{th} ring is computed from

$$G_i = e^{(\overline{\ln P(\theta_i)})} = e^{\left(\frac{1}{N_{obs}} \sum_{j=1}^{N_{obs}} \ln \frac{B_{ij}}{A_{ij}}\right)} \quad \text{Eq. (8)}$$

Assuming the foliage elements are randomly distributed in space, the effective PAI (PAI_{eff}) can be estimated by the transmittance in the different view angles based on Miller's formula (Miller, 1967).

$$PAI_{eff} = 2 \int_0^{\pi/2} -\ln P(\theta) \cos \theta \sin \theta d\theta \quad \text{Eq. (9)}$$

The amount of foliage in a vegetative canopy can be deduced from measurements of how quickly radiation is attenuated as it passes through the canopy. By measuring this attenuation at several angles from the zenith, foliage orientation information can also be obtained. The LAI-2200 measures the attenuation of diffuse sky radiation at five zenith angles simultaneously, arranged in concentric rings.

A normal measurement with the LAI-2200 consists of a minimum of ten numbers: five of the numbers are the signals from the five detectors when the optical sensor was above the vegetation, and the remaining five are the readings made with the sensor below the vegetation. For both readings, the sensor is looking up at the sky. Five values of canopy transmittance are calculated from these readings by dividing corresponding pairs.



Figure 5: LAI-2000 device (left) and LAI-2200C device (right).

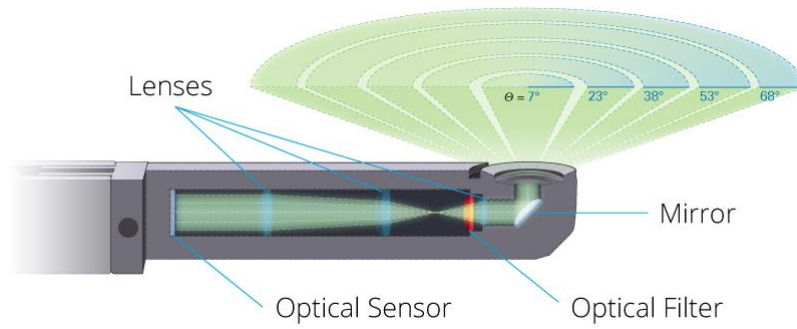


Figure 6: LAI-2200 optical sensor with 5 zenith angles

4.1.4. Mobile app: PocketLAI

The *PocketLAI* is an application developed for estimating LAI using a smartphone (Canfalonieri et al., 2013). It is an implementation of a simplified model of light transmittance based on the assumption of a random spatial distribution of infinitely small leaves. In this case, the gap fraction $P_0(\theta_\vartheta, \varphi_\vartheta)$ in direction of the zenith angle (θ_ϑ) and azimuth angle (φ_ϑ) is:

$$P_0(\theta_\vartheta, \varphi_\vartheta) = \exp \left[-G(\theta_\vartheta, \varphi_\vartheta) \frac{LAI}{\cos(\theta_\vartheta)} \right] \quad \text{Eq. (10)}$$

where $G(\theta_\vartheta, \varphi_\vartheta)$ is the projection function, i.e., the mean projection of a unit foliage area in the direction $(\theta_\vartheta, \varphi_\vartheta)$, which depends on the leaf angle distribution of the canopy. As discussed by Weiss et al. (2004), it was shown (Warren-Wilson, 1963) that for a view angle of 57.5° the G-function can be considered as almost independent of leaf inclination ($G \cong 0.5$). So that, by inversion of the model of Eq. (10), we can obtain LAI from the gap fraction measured at 57.5° :

$$LAI = - \left(\frac{\cos(57.5^\circ)}{0.5} \right) \log(P_0(57.5^\circ)) \quad \text{Eq. (11)}$$

4.2. SPATIAL SAMPLING SCHEME

All the sampled ESUs on vegetation correspond to different rice croplands. Furthermore, 6 ground control points (GCPs) over bare areas were added in order to extend the sampling over non vegetated areas. A pseudo-regular sampling was used within each ESU of approximately $20 \times 20 \text{ m}^2$. The centre of the ESU was geo-located. The sampling within the ESU varies depending on the instrument:

For DHP, 12 replications were conducted within the ESU, as with the LAIPocket app. For LAI-2000 or LAI-2200, 16 measurements (2×8) were carried out within the

ESU, whereas for AccuPAR, 27 (3 x 9) replications were performed to get the ESU value.

Table 4 shows the total number of ESU's for each campaign, and the instruments used in each campaign. Larger numbers of ESUs were characterized with more devices in those campaigns where both teams (UV and EOLAB) participated (17th of June, 15th of July and 8th of August). The UV team performed measurements with DHP, LAI-2000 and PocketLAI app regularly in about 20 ESUs per campaign. The EOLAB team measured with DHP, ceptometer and LAI-2200 in three campaigns (LAI-2200 was available only in the last campaign), increasing the number of rice plots sampled till about 35 ESUs. Note that during the join campaigns, inter-comparison of all the different devices were performed in several ESUs of different crops (around 10 ESUs per campaign). The largest intercomparison dataset was performed for effective LAI where DHP, LAI-2000 and PocketLAI app were obtained in all campaigns.

Figure 7 represents the distribution of the ESU's around the study area.

Table 4: Instruments used and total number of ESU's per campaign.

CAMPAIGN	DATE	LAI Pocket	ACCU - PAR	LAI - 2000	LAI - 2200	DHP-N	DHP-C	TOTAL OF ESU's (soil ESU'S)
1 st (C1)	06/17/2014	✓	✓	✓	X	✓	✓	39 (6)
2 nd (C2)	06/24/2014	✓	X	✓	X	✓	X	26 (6)
3 rd (C3)	06/29/2014	✓	X	✓	X	✓	X	26 (6)
4 th (C4)	07/06/2014	✓	X	✓	X	✓	X	25 (6)
5 th (C5)	07/15/2014	✓	✓	✓	X	✓	✓	42 (6)
6 th (C6)	07/22/2014	✓	X	✓	X	✓	X	31 (6)
7 th (C7)	07/31/2014	✓	X	✓	X	✓	X	31 (6)
8 th (C8)	08/07/2014	✓	✓	✓	✓	✓	✓	43 (6)
9 th (C9)	08/22/2014	✓	X	✓	X	✓	X	31 (6)



Figure 7: Distribution of the sampling units (ESU) over the study area. La Albufera site (Spain), 2014.

4.3. GROUND DATA

4.3.1. Data processing

The software CAN-EYE version V6.1 was used to process the DHP images. Figure 8 shows an example of the results of the CAN-EYE processing carried out on one rice ESU. Different results of the CAN-EYE processing are selected: the masking, the classification of vegetation and the image generated by the software. The average gap fraction and the clumping factor versus view zenith angle graphs are also shown.

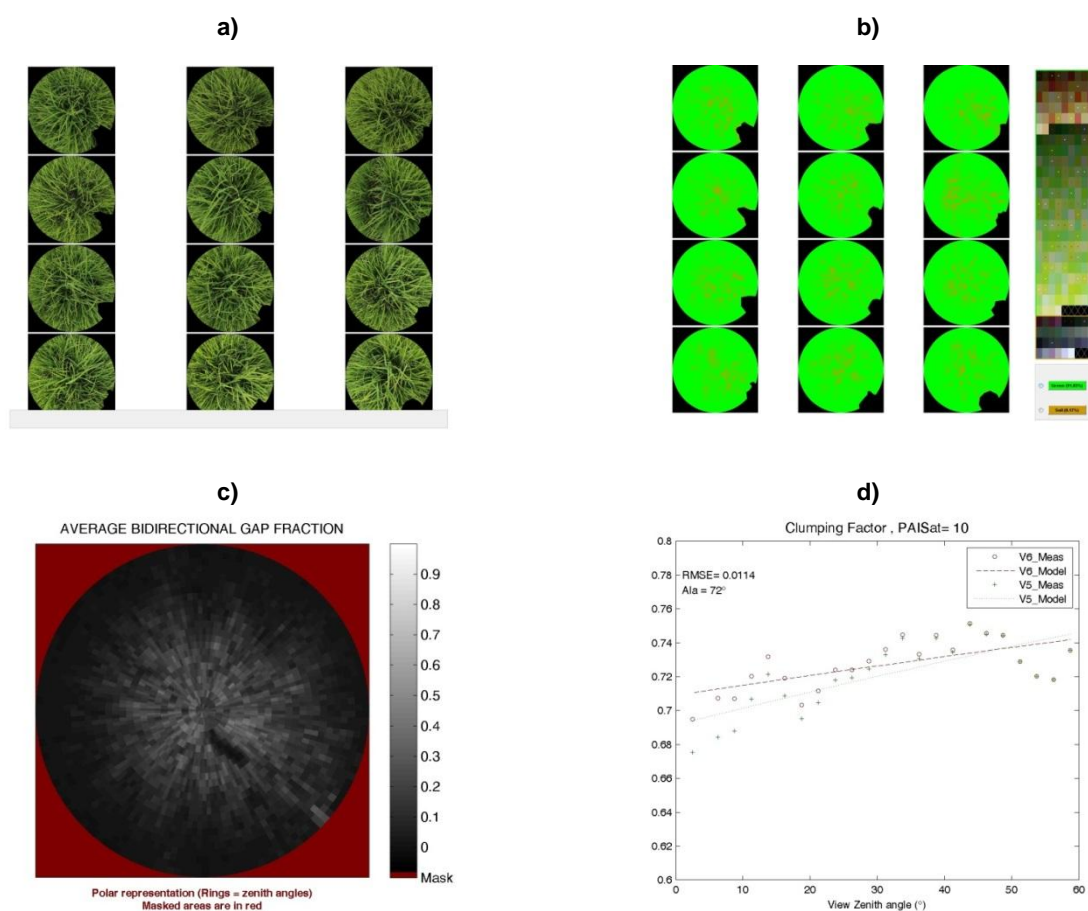


Figure 8: Example of the CAN-EYE processing carried out on rice ESU. a) DHP images. b) Classified images. c) Average gap fraction. d) Clumping factor versus view zenith angle.

- **DHP underestimation problems for FCover**

The analysis of the hemispherical photos processed with CAN-EYE showed in some cases unrealistically low values for FCover, as compared to the coverage what we observed in the field, and captured in the picture. Figure 9 shows an example of a very

dense rice canopy in our site, and the corresponding processing performed with CAN-EYE for retrieving biophysical variables. As can be observed, during the processing CAN-EYE identifies as vegetation green elements correctly, but however identify dark shadows as soil elements which is not exactly the case. In this case, rice plant elements present an electrophile distribution, and soil elements cannot be observed at densest stages. In this case, the vegetation produces a shadow that is projected over itself, hiding other green plant elements rather than soil. This is quite evident for FCover at nadir view around the center of the image, whereas for larger angular views shadows become less important. The result is an underestimation mainly of the FCover. Note that, in these cases, the surface reflectance signal sensed from space would correspond mostly to the contribution of the vegetation layer, with no contribution from soil elements. Thus, important differences with the DHP estimates may occur for densest rice canopies.

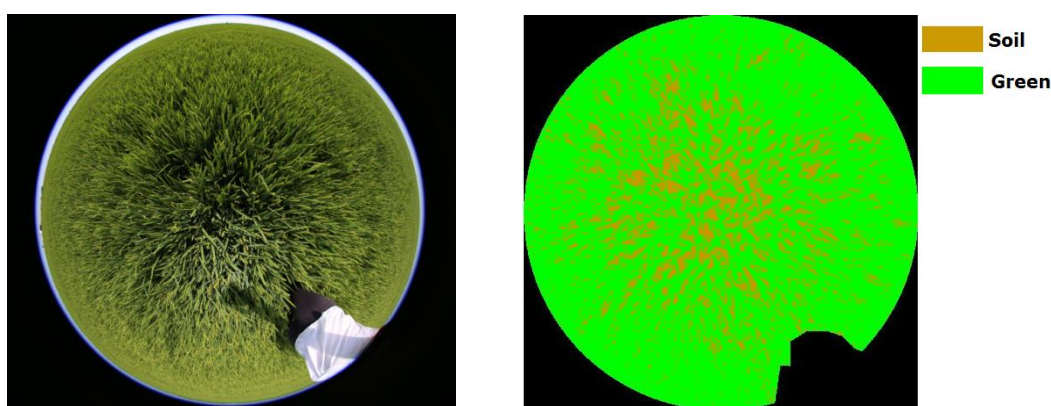


Figure 9: DHP picture and the result of the CAN-EYE processing for dense rice sample unit (ESU L6). La Albufera site (Spain), 2014.

We have analyzed the ground measurements, and discarded from the database the few cases with large discrepancies in the retrieved parameters (LAI, FAPAR) as compared to other devices, but the problem of the shaded vegetation identified as soil affects in some degree to most of the FCover values for the dense canopies. Therefore, the FCover data set should be used with caution, knowing that an underestimation is expected as compared to the complete coverage observed by the eye.

4.3.2. Inter-comparison of different instruments

Uncertainties attached to the obtained ground measurements with different instruments are investigated in this section comparing the different results.

An inter-comparison of LA_{eff} mean values, obtained by LAI-2000 and LAI-2200, DHP Canon (DHP-C), DHP Nikon (DHP-N), AccuPAR LP80 and *PocketLai*APP, for three ESUs (L1, L5 and L10) measured during three different campaigns in June, July and August, are depicted in Figure 10.

Similar mean results are obtained with the different instruments, with absolute differences typically lower than 0.5 LAI units, but that can go up to 1 when comparing some measurements (e.g., AccuPAR and LAI-2000 in July or LAI-2200 and DHP in August). The results were very consistent between the two LICORs in August, and also between the two DHPs in June and July. However, the DHPs showed larger discrepancies in August where DHP-C underestimates DHP-N retrievals. This can be explained by the impact of the subjective selection of green/soil elements introduced by the CAN-EYE operator for the classification of the digital image, which could be more important for densest canopies due to the difficulty to discriminate shaded vegetation as explained above. The PocketLAI App showed consistent results with the DHP, whereas the AccuPAR LP-80 tends to underestimate the DHP retrievals in agreement with the results obtained by Fang et al (2014b).

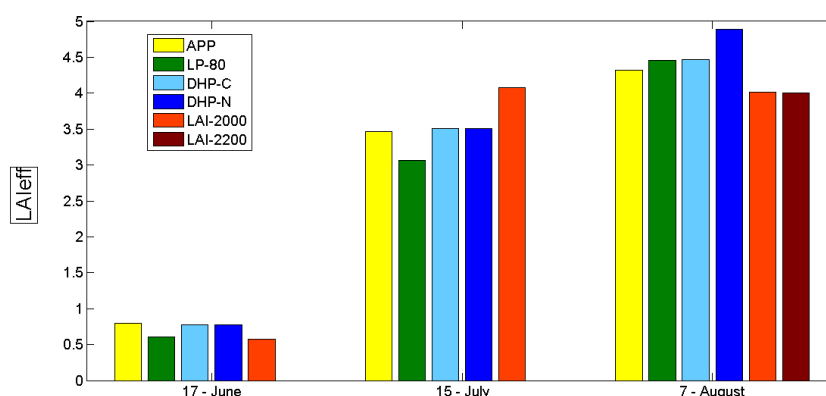


Figure 10: Mean LA_{eff} values derived using AccuPAR LP80, mobile APP, DHPs, LAI-2000 and LAI-2200 during the field campaign for 3 ESUs (L1, L5 and L10). La Albufera site (Spain), 2014.

Very consistent FAPAR mean values were obtained for ESUs L1, L5 and L10 (Figure 11). A little underestimation of DHP-C with respect to DHP-N can be observed again, which can be again explained due to the subjective selection of green/soil elements during the processing with the CAN-EYE software. The ceptometer LP-80 provides consistent estimates with DHP.

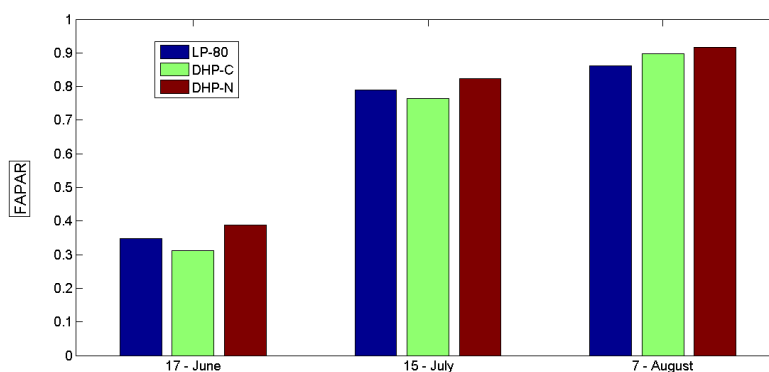


Figure 11: Mean FAPAR values derived using AccuPAR LP-80, DHP-C and DHP-N during the field campaign for 3 ESUs (L1, L5 and L10). La Albufera site (Spain), 2014.

Figure 12 shows the scatter-plots inter-comparing the measurements performed with different devices for the three campaigns where all the devices were available

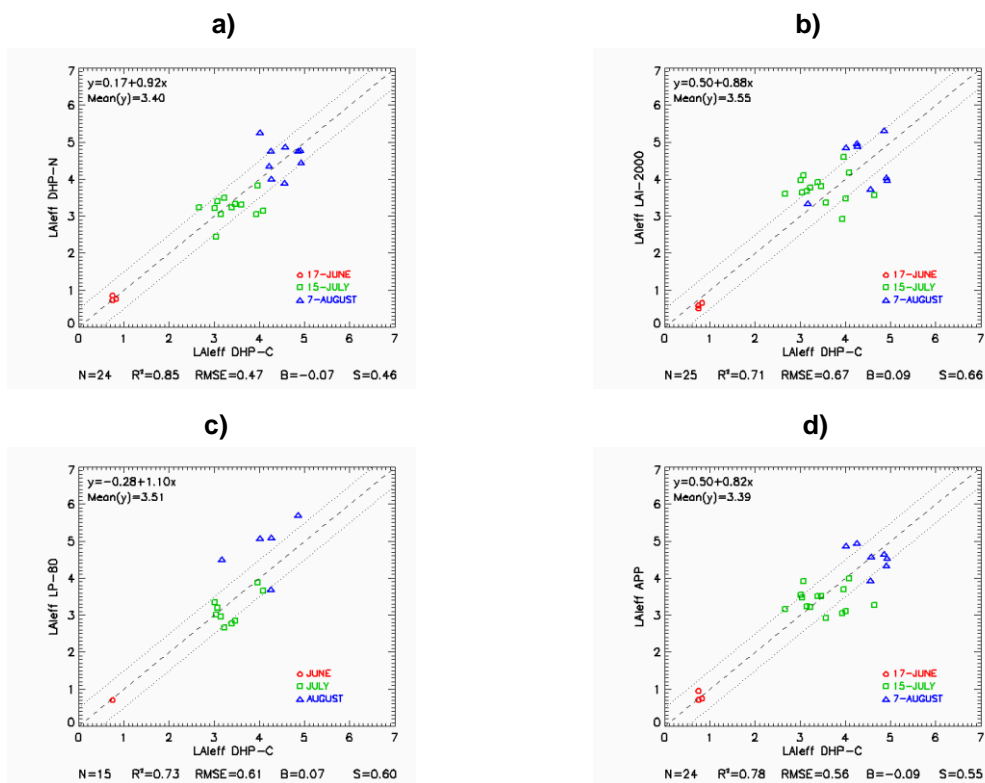


Figure 12: Scatter plots of LAleff values measured with different devices. a) DHP-C vs DHP-N. b) DHP-C vs LAI2000. c) DHP-C vs LP-80. d) DHP-C vs APP. La Albufera site (Spain), 2014.

For the LA_{eff} the different measurements were found quite consistent showing very little systematic differences among the different devices. However, some scattering was observed mainly between instruments. The overall error (RMSE) ranges between 0.47 and 0.67 LAI units. Similar results were obtained for the LAI (Figure 13) between the two DHP instruments, with negative bias and some scattering (RMSE=0.63).

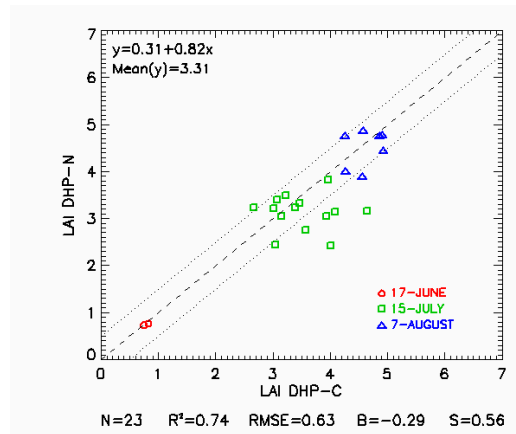


Figure 13: Scatter plots of LAI measured with 2 different DHP devices. La Albufera site (Spain), 2014.

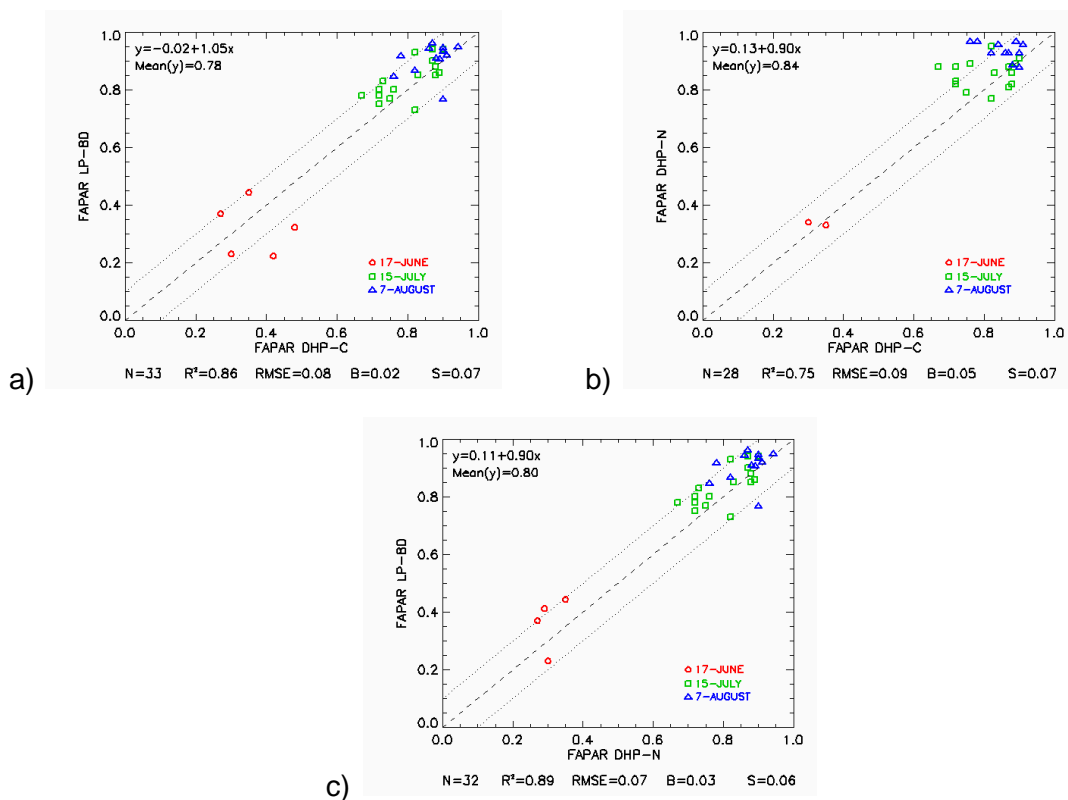


Figure 14: Scatter plots of FAPAR measured with different devices. a) DHP-C vs LP-80. b) DHP-C vs DHP-N. c) DHP-N vs LP-80. La Albufera site (Spain), 2014.

For the FAPAR, the agreement is quite good for the two DHP systems and the ceptometer. The correlation is high, with systematic errors lower than 0.05 and overall errors ranging between 0.07 and 0.09 (Figure 14).

Figure 15 shows scatter plot of FCOVER measurements between the two DHPs. As we commented in previous section, FCOVER values obtained with DHP-C are a little bit lower than values obtained with DHP-N ($B=0.08$), with an overall error of 0.11 and a good correlation ($R^2=0.74$).

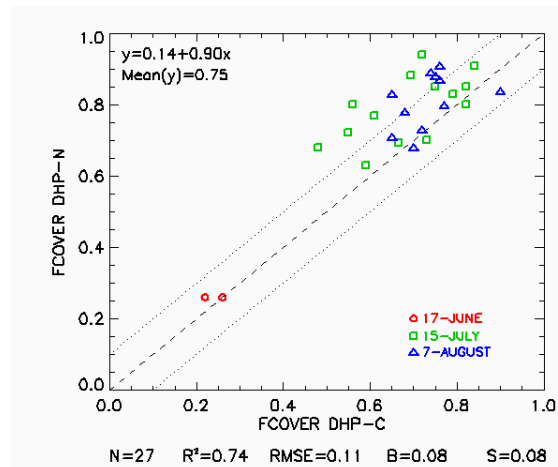


Figure 15: Scatter plots of F FCOVER measured values with DHP-C and DHP-N. La Albufera site (Spain), 2014

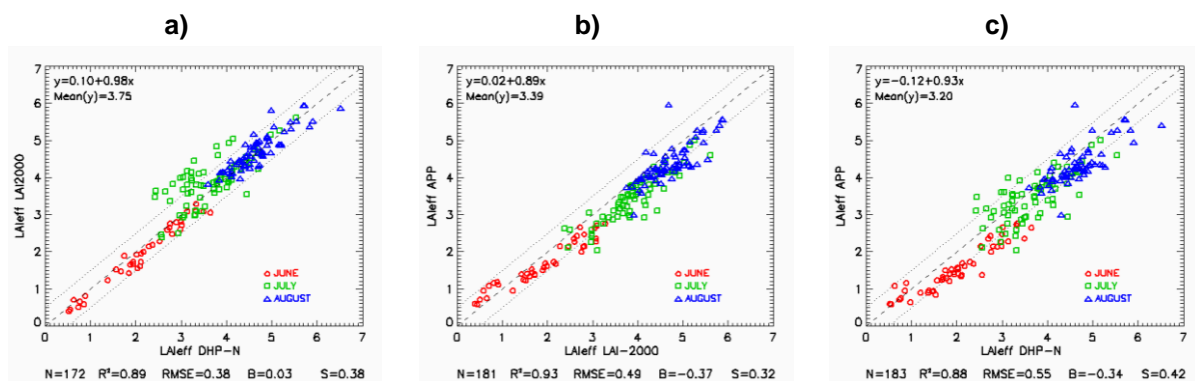


Figure 16: Scatter plots of LAleff for 3 instruments: a) DHP-N vs LAI-2000, b) LAI-2000 vs APP, c) DHP-N vs APP. Albufera Site (Spain), 2014.

LAleff is the only variable that has been measured in all the campaigns. So, a more consistent comparison between DHP-N, LAI-2000 and the mobile APP was obtained. Figure 16 shows the scatter plots between these 3 instruments for LAleff measurements. Note that the different campaigns have been gathered in months (June, July, and August) to obtain a better visualization of the results. The best

correlation of values can be observed between DHP-N and LAI-2000. Despite of some lower values of DHP-N with respect to LAI-2000, especially in July, low values of RMSE and BIAS (0.38 and 0, respectively) was obtained. A good performance (RMSE=0.49) can also be observed between LAI-2000 and PocketLAI App, but here a negative bias (-0.37) indicates that the PocketLAI tends to underestimate LAI-2000 values. Finally, the scatter plot of DHP-N versus the PocketLAI shows larger error (RMSE = 0.55) with a systematic bias (again PocketLAI provides lower values).

4.3.3. Content of the Ground Dataset

Each ESU is described according to a standard format. The header of the database is shown in Table 5.

Table 5: Header used to describe ESUs with the ground measurements.

Column	Var. Name	Comment	
1	Plot #	Number of the field plot in the site	
2	Plot Label	Label of the plot in the site	
3	ESU #	Number of the Elementary Sampling Unit (ESU)	
4	ESU Label	Label of the ESU in the campaign	
5	Northing Coord.	Geographical coordinate: Latitude (°), WGS-84	
6	Easting Coord.	Geographical coordinate: Longitude (°), WGS-84	
7	Extent (m) of ESU (diameter)	Size of the ESU ⁽¹⁾	
8	Land Cover	Detailed land cover	
9	Start Date (dd/mm/yyyy)	Starting date of measurements	
10	End Date (dd/mm/yyyy)	Ending date of measurements	
11	Products*	Method	Instrument
12		Nb. Replications	Number of Replications
13		PRODUCT	Methodology
14		Uncertainty	Standard deviation

*LAI_{eff}, LAI, FAPAR at 10:00, FCOVER and FAPAR Daily Integrated.

Figure 17 shows the mean values and standard deviation of measurements obtained during the field experiment. A quick increase of the values is observed during the first 5 campaigns (from 17th June to 15th July) and after that, LAI_{eff} values become stabilized, whereas FAPAR, FCOVER and LAI continue increasing, but more slowly. The observed differences between the LAI_{eff} and the LAI are larger at the end of the growing season, due to the evolution of the clumping of foliage during the season. The clumping index ranges from 0.87 in June to 0.74 in August with 0.80 in July, and so the differences between LAI and LAI_{eff} are larger at the end of the season (Eq. 2). These

results are consistent with that reported by Fang et al., (2014a) over paddy rice fields, with clumping index values estimated from downward looking pictures ranging from 0.80 to 0.74 from the beginning to the end of the rice cycle. Note however that higher clumping index values (around 0.65) were estimated using upward looking pictures instead of downward looking (Fang et al., 2014a). The uncertainty attached to the clumping index should be further investigated.

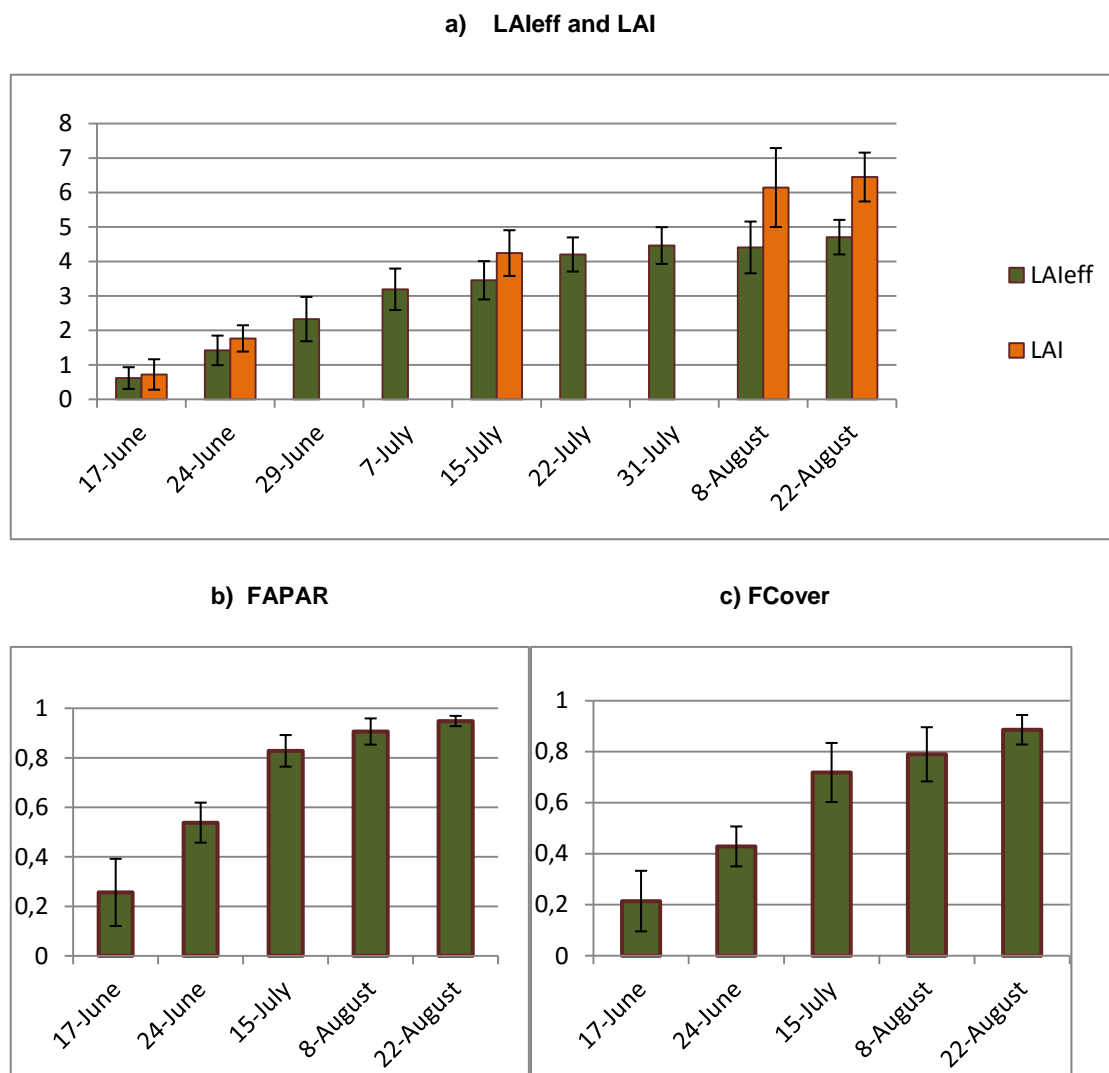


Figure 17: Mean values and standard deviation: a) LA_{eff} and LAI. b) FAPAR at 10:00. c) FCover. Albufera site (Spain), 2014.

Histograms of ground measurements for different biophysical variables are depicted in Figure 18 and Figure 19. Here can be observed again that LA_{eff} values have tended to stabilize after 22nd of July.

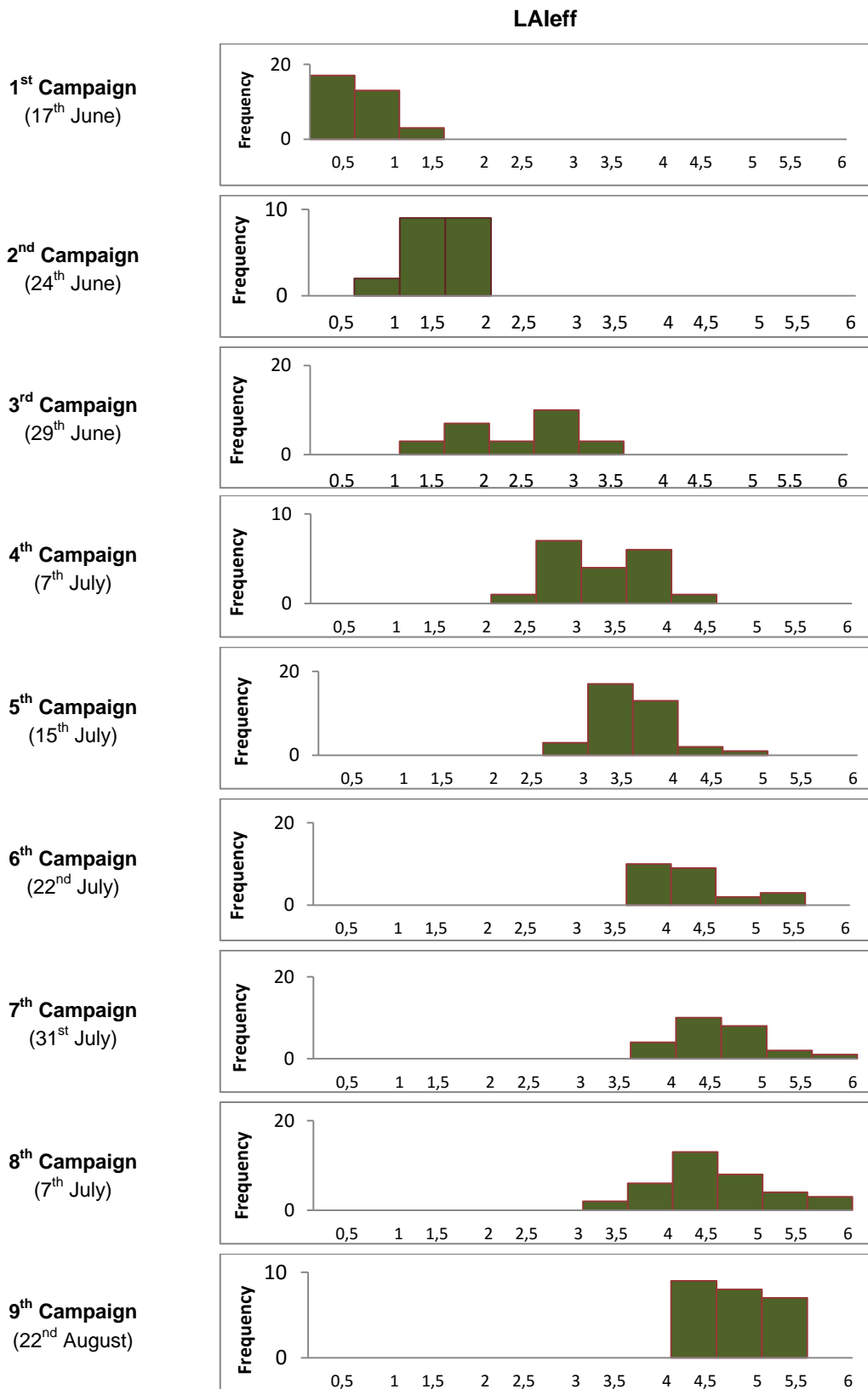


Figure 18: Histograms of LAleff ground data measurements for different campaigns. Albufera site (Spain), 2014.

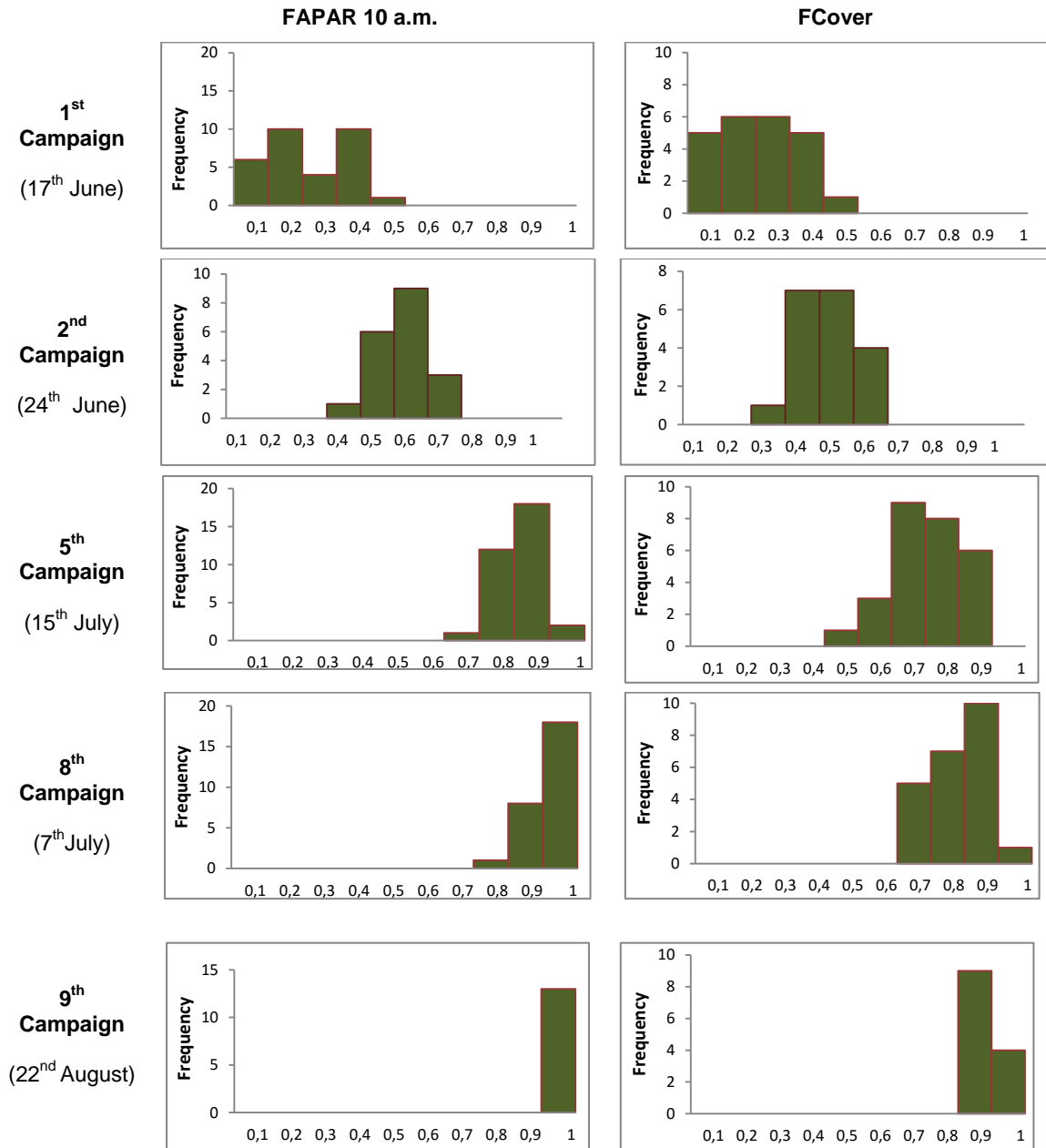


Figure 19: Histograms of FAPAR at 10:00 a.m. and FCover ground data measurements for different campaigns. Albufera site (Spain), 2014.

5. EVALUATION OF THE SAMPLING

5.1. PRINCIPLES

Based on previous field activities, the sampling was concentrated in the most representative areas where farmers provided access to their fields. The number of ESUs of each campaign is indicated in the next table. This number includes 6 soil ESUs in all the campaigns. Table 6 summarizes the number of ESUs per campaign.

Table 6: Number of ESUs per campaign.

	17 th June	24 th June	29 th June	6 th July	15 th July	22 nd July	31 st July	7 th August	22 nd August
No. of ESUs	39	26	26	25	42	31	31	43	31

5.2. EVALUATION BASED ON NDVI VALUES

The sampling strategy is evaluated using the Landsat-8 image by comparing the NDVI distribution over the site with the NDVI distribution over the ESUs (Figure 20). As the number of pixels is drastically different for the ESU and whole site (20x20 km²), It is not statistically consistent to directly compare the two NDVI histograms. Therefore, the proposed technique consists in comparing the NDVI cumulative frequency of the two distributions by a Monte-Carlo procedure which aims at comparing the actual frequency to randomly shifted sampling patterns. It consists in:

1. Computing the cumulative frequency of the N pixel NDVI that correspond to the exact ESU locations; then, applying a unique random translation to the sampling design (modulo the size of the image)
2. Computing the cumulative frequency of NDVI on the randomly shifted sampling design
3. Repeating steps 1 and 2, 199 times with 199 different random translation vectors.

This provides a total population of $N = 199 + 1$ (actual) cumulative frequency on which a statistical test at acceptance probability $1 - \alpha = 95\%$ is applied: for a given NDVI level, if the actual ESU density function is between two limits defined by the $N\alpha/2 = 5$ highest and lowest values of the 200 cumulative frequencies, the hypothesis assuming that whole site and ESU NDVI distributions are equivalent is accepted, otherwise it is rejected.

Figure 20 shows that the NDVI TOA distribution of the La Albufera site. The sampling presents a slight bias towards higher NDVI values for campaigns of July and August. This result was expected because all the measured values were obtained in rice crops, and the image represents an area with other surfaces, like water, urban areas and bare areas. Because of the presence of water, only the cumulative histograms of our sampling and the sampling over maximum values are represented.

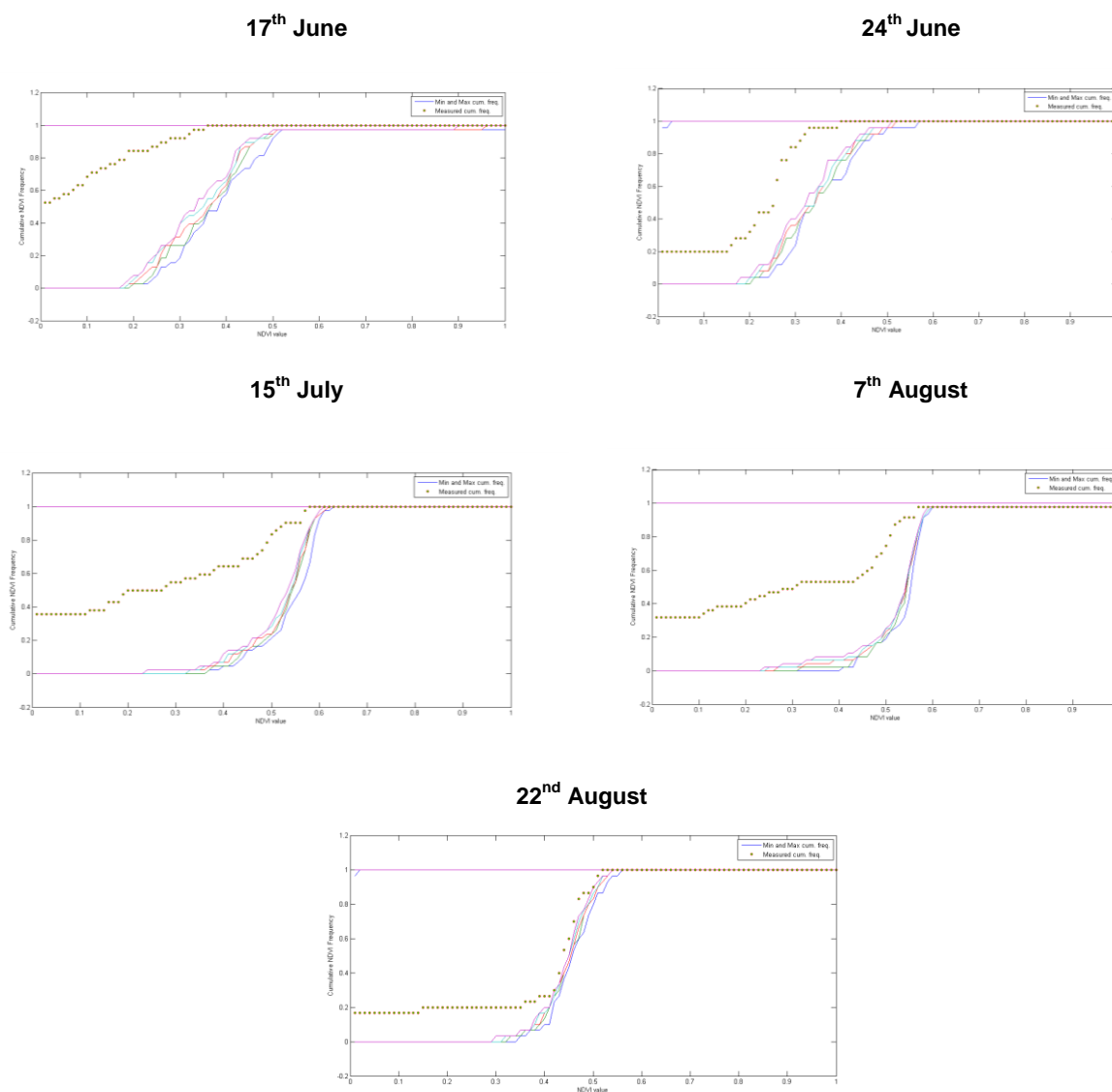


Figure 20: Comparison of NDVI (TOA) distribution between ESUs (green dots) and over the whole image (Blue line). Albufera site (Spain), 2014.

5.3. EVALUATION BASED ON CONVEX HULL: PRODUCT QUALITY FLAG.

The interpolation capabilities of the empirical transfer function used for up-scaling the ground data using decametric images is dependent of the sampling (Martinez et al., 2009). A test based on the convex hulls was also carried out to characterize the representativeness of ESUs and the reliability of the empirical transfer function using the different combinations of the selected bands (green, red, NIR and SWIR) of the Landsat-8 image. A flag image is computed over the reflectances. The result on convex-hulls can be interpreted as:

- Pixels inside the 'strict convex-hull': a convex-hull is computed using all the Landsat-8 reflectances corresponding to the ESUs belonging to the class. These pixels are well represented by the ground sampling and therefore, when applying a transfer function the degree of confidence in the results will be quite high, since the transfer function will be used as an interpolator;
- Pixels inside the 'large convex-hull': a convex-hull is computed using all the reflectance combinations ($\pm 5\%$ in relative value) corresponding to the ESUs. For these pixels, the degree of confidence in the obtained results will be quite good, since the transfer function is used as an extrapolator (but not far from interpolator);
- Pixels outside the two convex-hulls: this means that for these pixels, the transfer function will behave as an extrapolator which makes the results less reliable. However, having a priori information on the site may help to evaluate the extrapolation capacities of the transfer function.

Figure 21 shows the results of the Convex-Hull test (i.e., Quality Flag image) for the Albufera site over a $20 \times 20 \text{ km}^2$ area around the central coordinate site. The strict and large convex-hulls are high around the test site, between 82% and 86% in the $5 \times 5 \text{ km}^2$ area around the central pixel (Yellow square) and even more higher (between 88% and 93%) for the $3 \times 3 \text{ km}^2$ area used for validation of 1 km satellite products.

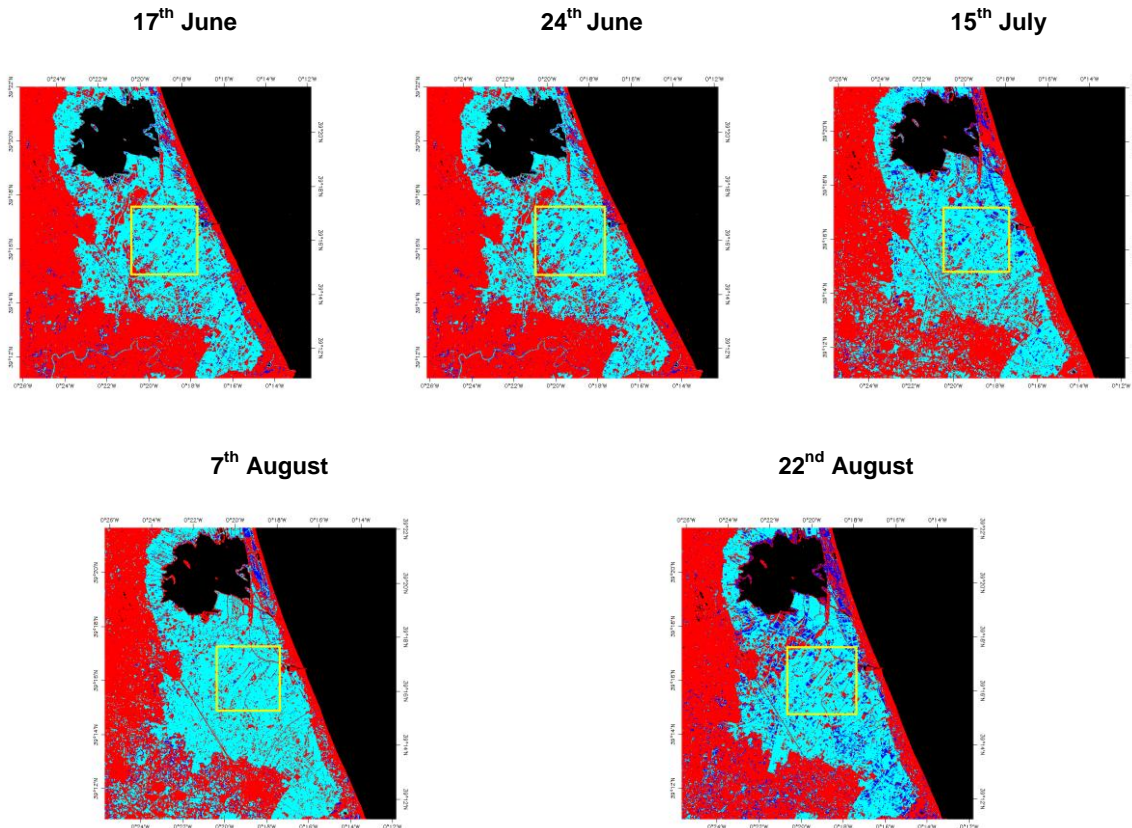


Figure 21: Convex Hull test over 20x20km² area centered at the test site: clear and dark blue correspond to the pixels belonging to the 'strict' and 'large' convex hulls, red corresponds to the pixels for which the transfer function is extrapolating and black pixels represent water bodies. Yellow square marks the 5x5km² study area. Albufera site (Spain), 2014.

6. PRODUCTION OF GROUND-BASED MAPS

6.1. IMAGERY

The ground estimated values were up-scaled using Landsat-8 imagery and empirical transfer function for 5 field campaigns where cloud-free images were available (Table 7).

Table 7: Landsat-8 cloud-free images available.

CAMPAIGN	FIELD CAMPAIGN DATES	IMAGERY DATES
1 st campaign	2014.06.17	2014.06.20
2 nd campaign	2014.06.24	2014.06.20
5 th campaign	2014.07.15	2014.07.15
8 th campaign	2014.08.07	2014.07.31
9 th Campaign	2014.08.22	2014.09.01

All the images were acquired close to the field acquisition (one week), except for the last campaign where the shift is 10 days and possible changes in the structure of the rice field could happen.

Four cloud-free Landsat-8 images have been acquired on the dates 20th of June, 15th of July, 31th of July and 1st of September 2014. Four Landsat-8 spectral bands of TOA reflectance were used from 500 nm to 1650 nm with a nadir ground sampling distance of 30 m. The projection of the image of 20th of June is UTM 30 North, WGS84, whereas the projection of the rest of images is UTM 31 North, WGS84, as the site falls in the overlap region of two different orbits, and is located close to the limit between UTM30 and UTM 31 zones.

No atmospheric correction was applied to the images. Thus, Landsat-8 TOA reflectance images are used to compute empirical relationships between reflectance and biophysical variable, we assume that the effect of the atmosphere is the same over the whole site.

Table 8: Characteristics of Landsat-8 input data imagery.

Landsat-8 METADATA					
Platform / Instrument	Landsat-8/ OLI_TIRS				
Sensor	OPTICAL 30 m				
Spectral Range (selected bands)	B3(green) : 0.53-0.59 μm B4(red) : 0.64-0.67 μm B5(NIR) : 0.85-0.88 μm B6(SWIR1) : 1.58-1.65 μm				
	First Campaign (17 th June, 2014)	Second Campaign (24 th June, 2014)	Fifth Campaign (15 th July, 2014)	Eighth Campaign (7 th August, 2014)	Ninth Campaign (22 nd August, 2014)
Acquisition date	2014/06/20	2014/06/20	2014/07/15	2014/07/31	2014/09/01
Illumination Azimuth angle	124.94°	124.94°	126.41°	131°	143.89°
Illumination Elevation angle	66.69°	66.69°	64.61°	62.06°	54.49°
Ground Control Points verify	129	129	53	78	99
Geometric RMSE verify	4.214	4.214	4.491	4.468	6.038
Projection	UTM 30 North, WGS84	UTM 30 North, WGS84	UTM 31 North, WGS84	UTM 31 North, WGS84	UTM 31 North, WGS84

6.2. THE TRANSFER FUNCTION

6.2.1. The regression method

If the number of ESUs is enough, multiple robust regressions 'REG' between ESUs reflectance and the considered biophysical variable can be applied (Martínez et al., 2009): we used the 'robustfit' function from the Matlab statistics toolbox. It uses an iteratively re-weighted least squares algorithm, with the weights at each iteration computed by applying the bi-square function to the residuals from the previous iteration. This algorithm provides lower weight to ESUs that do not fit well.

The results are less sensitive to outliers in the data as compared with ordinary least squares regression. At the end of the processing, two errors are computed: weighted RMSE (RW) (using the weights attributed to each ESU) and cross-validation RMSE (RC) (leave-one-out method).

As the method has limited extrapolation capacities, a flag image (Figure 21), based on the convex hulls is included in the final ground based map in order to inform the users on the reliability of the estimates.

6.2.2. Band combination

Figure 22 to Figure 26 represent the test of multiple regressions (Transfer Function) applied on different band combinations for each campaign and variable. Attending specifications of lower RMSE, it has been chosen for all the campaigns:

band 4 (Short Wave Infrared), band 3 (Near Infrared), band 2 (Red) and band 1 (Green) combination.

In spite of the band combination of [4,3,2,1] doesn't give the lowest values of RC and RW in all the transfer functions (e.g. the band combination of [4,2] is a little bit lower than [4,3,2,1] in the first campaign), this combination on reflectance was selected for the transfer function since it provides a good compromise between the low cross-validation RMSE (RC), the weighted RMSE (RW) (lowest value) and the number of rejected points.

First Campaign (17th of June, 2014)

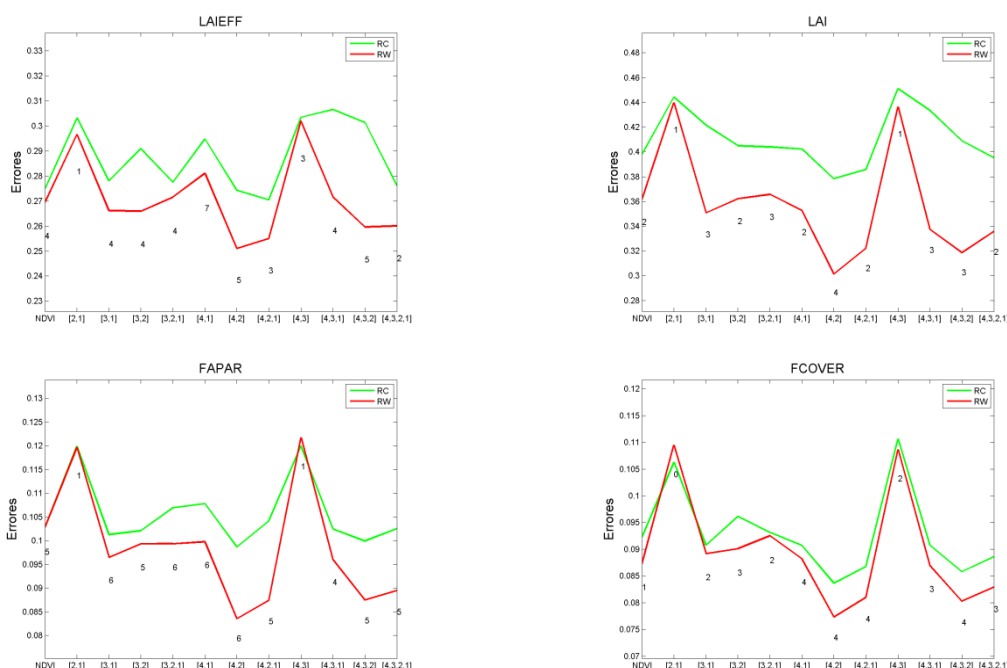


Figure 22: Test of multiple regressions (Transfer Function) applied on different band combinations. Band combinations are given in abscissa (1=G, 2=RED, 3=NIR and 4=SWIR). The weighted root mean square error (RW) is presented in red along with the cross-validation RMSE (RC) in green. First Campaign (2014.06.17), Albufera site (Spain), 2014.

Second Campaign (24th of June, 2014)

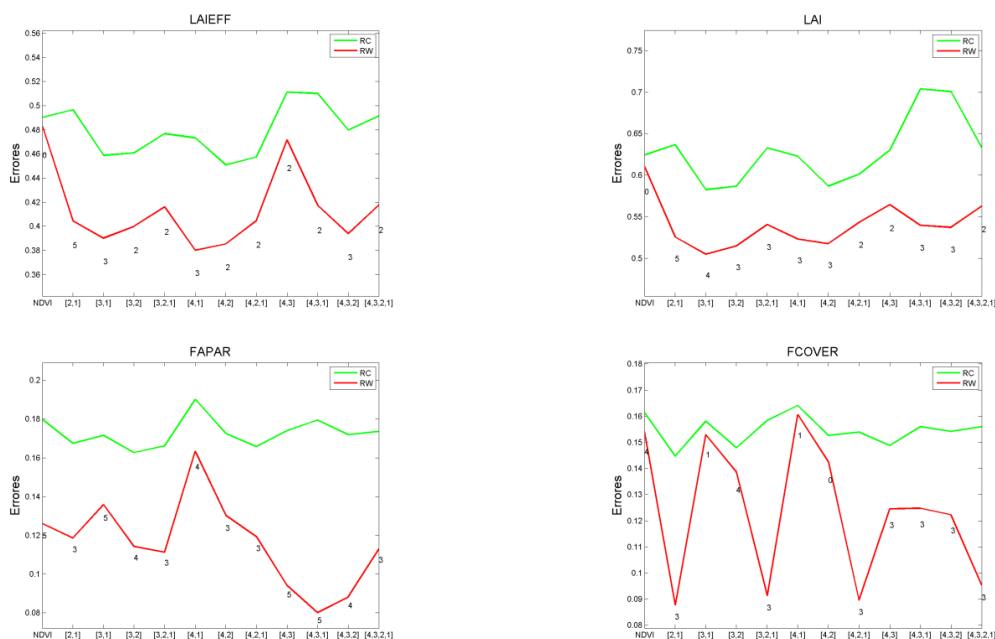


Figure 23: Test of multiple regressions (Transfer Function) applied on different band combinations. Band combinations are given in abscissa (1=G, 2=RED, 3=NIR and 4=SWIR). The weighted root mean square error (RW) is presented in red along with the cross-validation RMSE (RC) in green. Second Campaign (2014.06.24), Albufera site (Spain), 2014.

Fifth Campaign (15th of July, 2014)

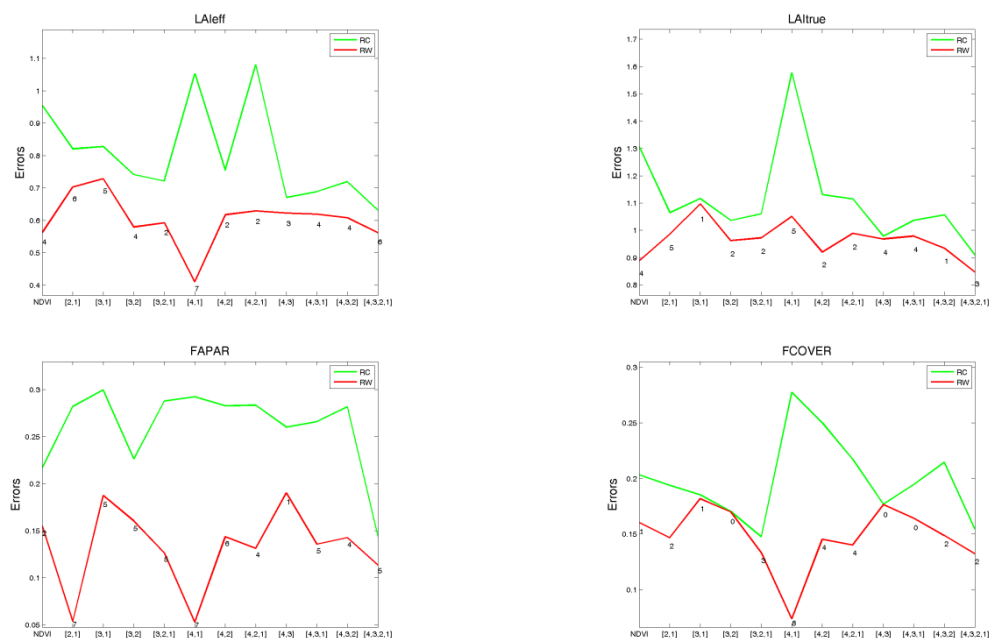


Figure 24: Test of multiple regressions (Transfer Function) applied on different band combinations. Band combinations are given in abscissa (1=G, 2=RED, 3=NIR and 4=SWIR). The weighted root mean square error (RW) is presented in red along with the cross-validation RMSE (RC) in green. Fifth Campaign (2014.07.17), Albufera site (Spain), 2014.

Eighth Campaign (7th of August, 2014)

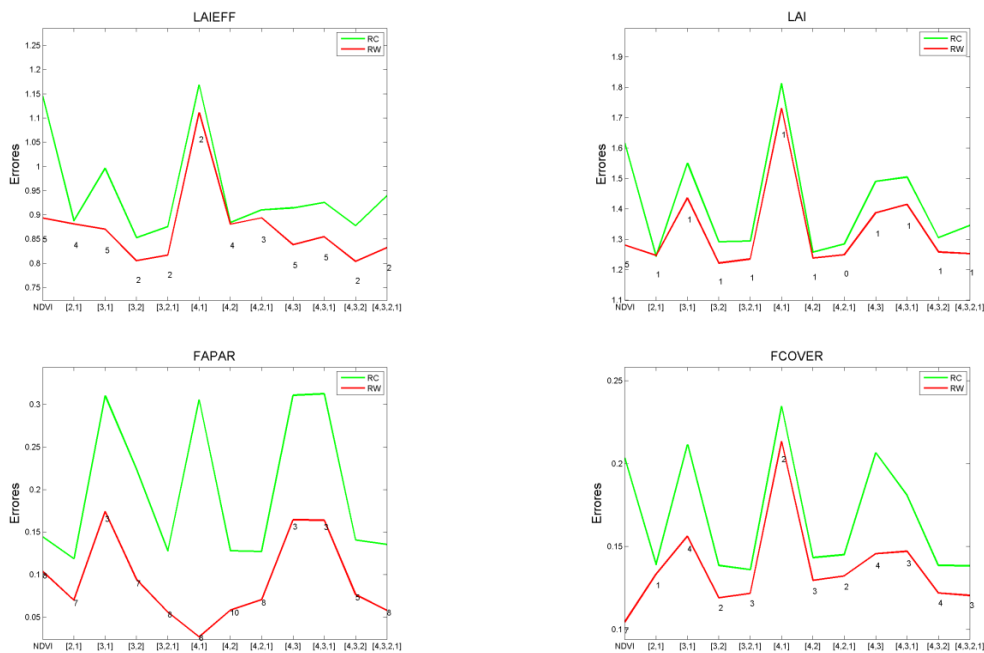


Figure 25: Test of multiple regressions (Transfer Function) applied on different band combinations. Band combinations are given in abscissa (1=G, 2=RED, 3=NIR and 4=SWIR). The weighted root mean square error (RW) is presented in red along with the cross-validation RMSE (RC) in green. Eighth Campaign (2014.08.07), Albufera site (Spain), 2014.

Ninth Campaign (22nd of August, 2014)

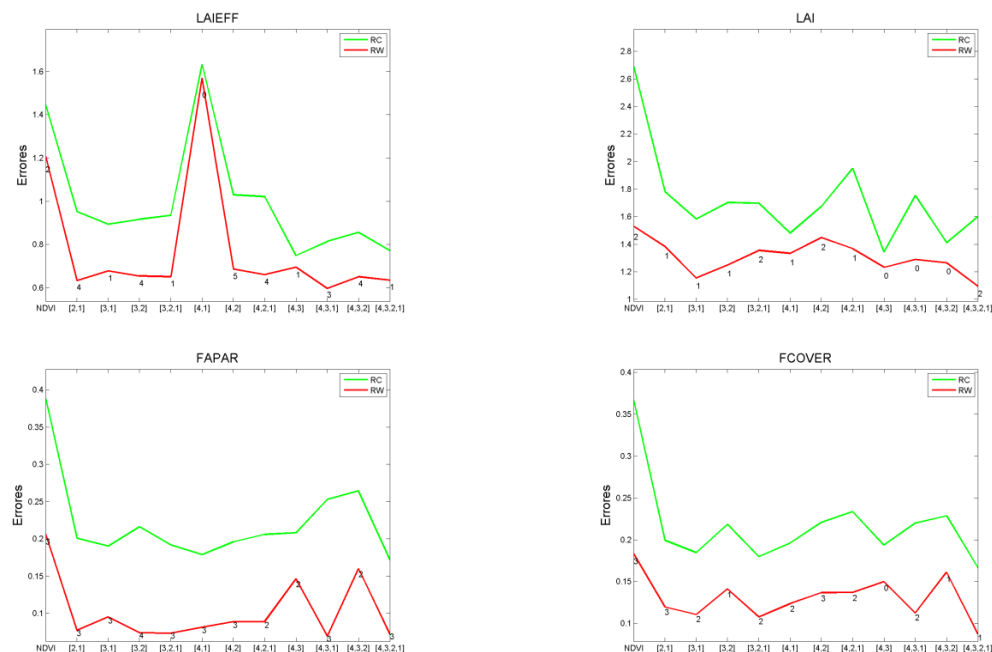


Figure 26: Test of multiple regressions (Transfer Function) applied on different band combinations. Band combinations are given in abscissa (1=G, 2=RED, 3=NIR and 4=SWIR). The weighted root mean square error (RW) is presented in red along with the cross-validation RMSE (RC) in green. Ninth Campaign (2014.08.22), Albufera site (Spain), 2014.

6.2.3. The selected Transfer Function

The applied transfer function is detailed in Table 9 and Table 10, along with its weighted and cross validated errors (RMSE).

Table 9: Transfer function applied to the whole site for LAleff, LAI, FAPAR 10:00 a.m. and FCover for campaigns of 17th June, 24th June, 15th July and 7th August and 22nd August 2014. RW stands for weighted RMSE, and RC stands for cross-validation RMSE.

Variable	Band Combination	RW	RC
17th June			
LAleff	$0.82833+0.000011 \cdot (\text{SWIR})+0.000009 \cdot (\text{NIR})-0.00051 \cdot (\text{R})+0.00033 \cdot (\text{G})$	0.26	0.267
LAI	$2.23868+0.00019 \cdot (\text{SWIR})-0.000032 \cdot (\text{NIR})-0.00063 \cdot (\text{R})+0.00025 \cdot (\text{G})$	0.336	0.378
FAPAR	$0.73706+0.000056 \cdot (\text{SWIR})-0.000008 \cdot (\text{NIR})-0.000203 \cdot (\text{R})+0.00008 \cdot (\text{G})$	0.089	0.099
FCover	$0.59510+0.000055 \cdot (\text{SWIR})-0.000012 \cdot (\text{NIR})-0.000198 \cdot (\text{R})+0.000098 \cdot (\text{G})$	0.083	0.084

Variable	Band Combination	RW	RC
24th June			
LAleff	$3.611436+0.000205 \cdot (\text{SWIR})-0.000084 \cdot (\text{NIR})-0.001047 \cdot (\text{R})+0.000608 \cdot (\text{G})$	0.395	0.424
LAI	$4.4976185+0.000066 \cdot (\text{SWIR})+0.00003 \cdot (\text{NIR})-0.000759 \cdot (\text{R})+0.000254 \cdot (\text{G})$	0.56	0.637
FAPAR	$-0.0645295-0.000029 \cdot (\text{SWIR})+0.000037 \cdot (\text{NIR})-0.000273 \cdot (\text{R})+0.00027 \cdot (\text{G})$	0.419	0.487
FCover	$-1.1438593+0.000003 \cdot (\text{SWIR})+0.0000025 \cdot (\text{NIR})-0.000451 \cdot (\text{R})+0.000551 \cdot (\text{G})$	0.117	0.169

Variable	Band Combination	RW	RC
15th July			
LAleff	$0.56182-0.00054 \cdot (\text{SWIR})+0.00032 \cdot (\text{NIR})-0.00057 \cdot (\text{R})+0.00066 \cdot (\text{G})$	0.562	0.619
LAI	$-0.77617-0.00075 \cdot (\text{SWIR})+0.00039 \cdot (\text{NIR})-0.00091 \cdot (\text{R})+0.00126 \cdot (\text{G})$	0.847	0.893
FAPAR	$-0.11585-0.000127 \cdot (\text{SWIR})+0.000056 \cdot (\text{NIR})-0.00028 \cdot (\text{R})+0.00035 \cdot (\text{G})$	0.113	0.136
FCover	$-1.34476-0.00013 \cdot (\text{SWIR})+0.00007 \cdot (\text{NIR})-0.00022 \cdot (\text{R})+0.000391 \cdot (\text{G})$	0.129	0.132

Variable	Band Combination	RW	RC
7th August			
LAleff	$8.97911-0.00021 \cdot (\text{SWIR})+0.00019 \cdot (\text{NIR})-0.00134 \cdot (\text{R})+0.00036 \cdot (\text{G})$	0.826	0.832
LAI	$14.63941+0.000007 \cdot (\text{SWIR})+0.00011 \cdot (\text{NIR})-0.00258 \cdot (\text{R})+0.00088 \cdot (\text{G})$	1.172	1.252
FAPAR	$1.87254-0.00005 \cdot (\text{SWIR})+0.000015 \cdot (\text{NIR})-0.00038 \cdot (\text{R})+0.000177 \cdot (\text{G})$	0.058	0.116
FCover	$1.09937-0.000034 \cdot (\text{SWIR})+0.000041 \cdot (\text{NIR})-0.000306 \cdot (\text{R})+0.00015 \cdot (\text{G})$	0.12	0.127

Table 10: Transfer function applied to the whole site for LAI_{eff}, LAI, FAPAR 10:00 a.m. and FCOVER for campaign of 22nd August 2014. RW stands for weighted RMSE, and RC stands for cross-validation RMSE.

Variable	Band Combination	RW	RC
22nd August			
LAI_{eff}	$8.3648404 - 0.001402 \cdot (\text{SWIR}) + 0.000647 \cdot (\text{NIR}) + 0.001637 \cdot (\text{R}) - 0.0016434 \cdot (\text{G})$	0.592	0.634
LAI	$22.381142 - 0.001639 \cdot (\text{SWIR}) + 0.000765 \cdot (\text{NIR}) + 0.0035179 \cdot (\text{R}) - 0.004686 \cdot (\text{G})$	1.095	1.612
FAPAR	$4.330063 - 0.00018 \cdot (\text{SWIR}) + 0.00008 \cdot (\text{NIR}) + 0.000495 \cdot (\text{R}) - 0.000785 \cdot (\text{G})$	0.072	0.169
FCover	$3.8875397 - 0.000168 \cdot (\text{SWIR}) + 0.000086 \cdot (\text{NIR}) + 0.000502 \cdot (\text{R}) + 0.000778 \cdot (\text{G})$	0.087	0.161

Figure 27 to Figure 31 show the scatter-plots between ground observations and their corresponding transfer function (TF) estimates for the selected band combinations. Mean values of the different device measurements available for each ESU were used.

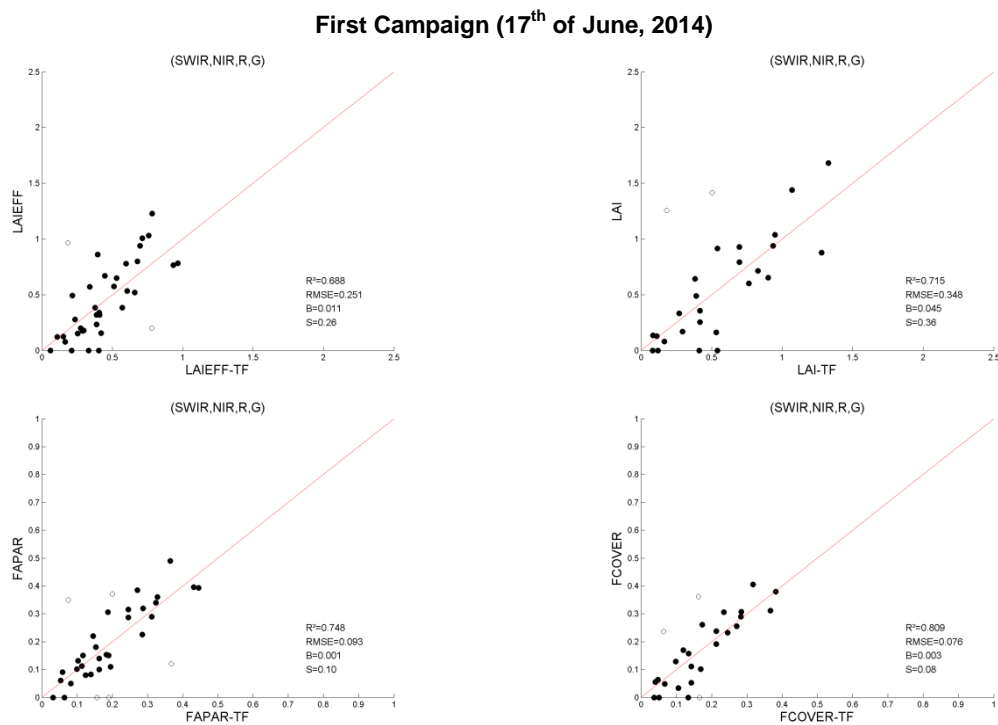


Figure 27: LAI_{eff}, LAI, FAPAR 10 a.m. and FCOVER results for regression on reflectance using 4 bands combination. First Campaign (2014.06.17), Albufera site (Spain), 2014.

Second Campaign (24th of June, 2014)

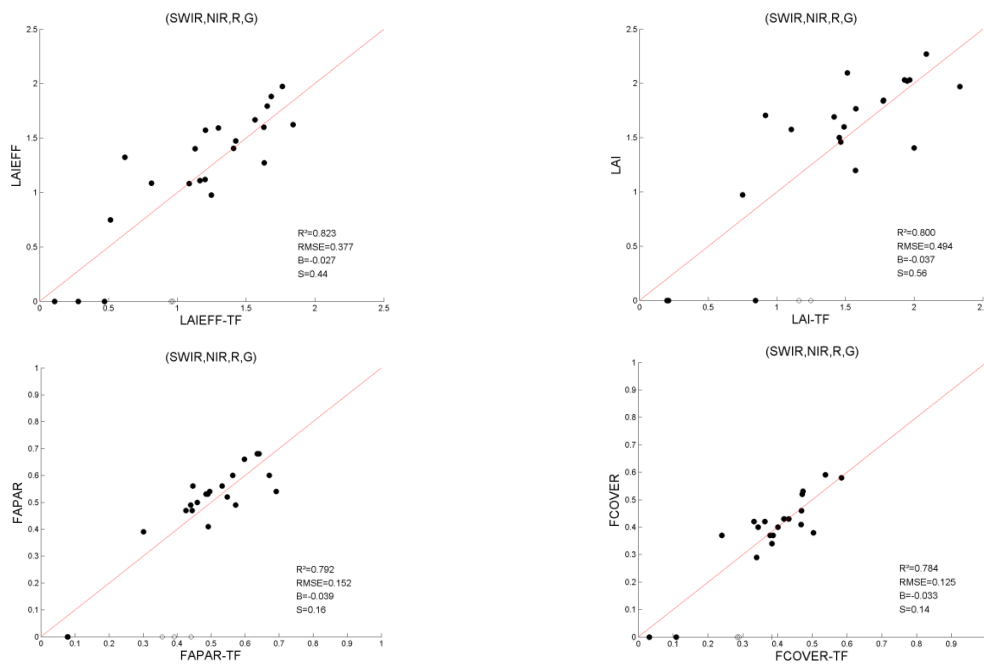


Figure 28: LAIEff, LAI, FAPAR 10 a.m. and FCOVER results for regression on reflectance using 4 bands combination. Second Campaign (2014.06.24), Albufera site (Spain), 2014.

Fifth Campaign (15th of July, 2014)

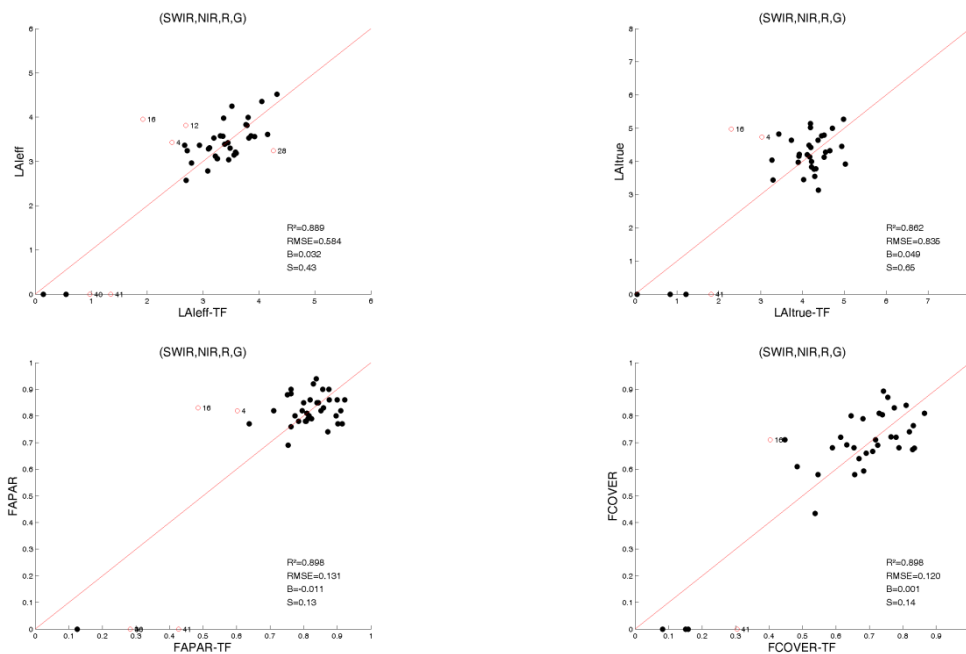


Figure 29: LAIEff, LAI, FAPAR 10 a.m. and FCOVER results for regression on reflectance using 4 bands combination. Fifth Campaign (2014.07.15), Albufera site (Spain), 2014.

Eighth Campaign (7th of August, 2014)

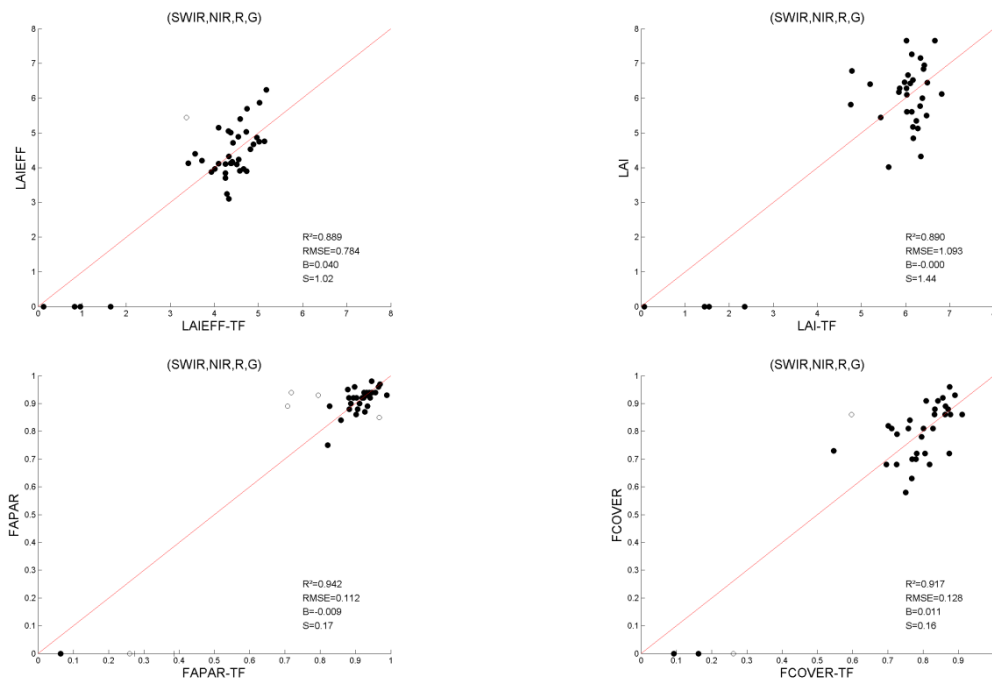


Figure 30: LAIEff, LAI, FAPAR 10 a.m. and FCOVER results for regression on reflectance using 4 bands combination. Eighth Campaign (2014.08.07), Albufera site (Spain), 2014.

Ninth Campaign (22nd of August, 2014)

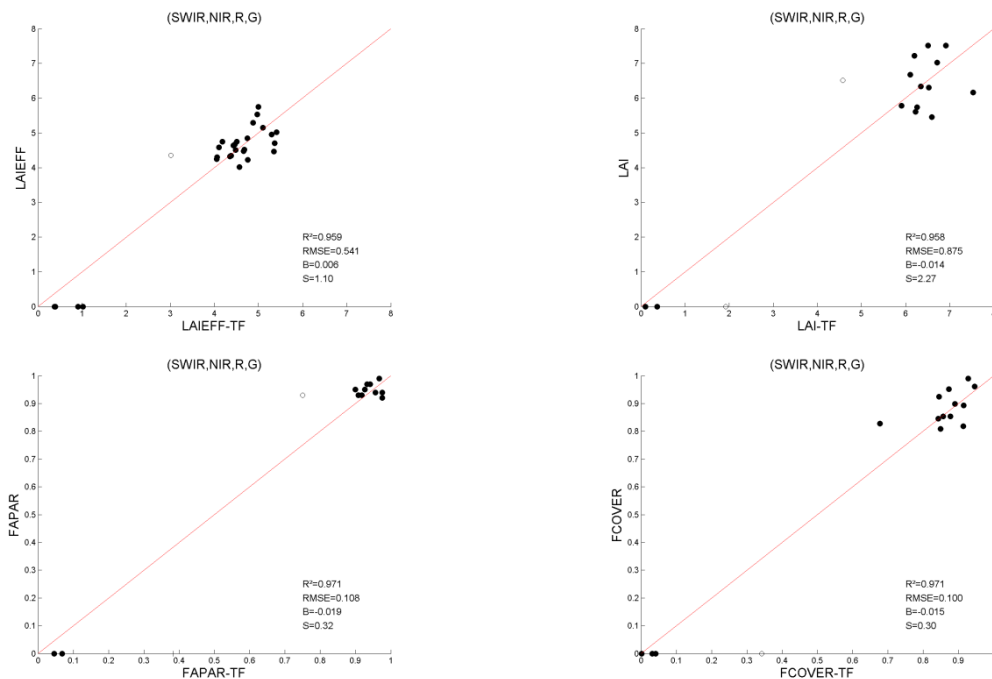


Figure 31: LAIEff, LAI, FAPAR 10 a.m. and FCOVER results for regression on reflectance using 4 bands combination. Ninth Campaign (2014.08.22), Albufera site (Spain), 2014.

In general, good agreement between ground data and transfer function estimates were obtained, with no systematic bias detected. Some scattering is observed however in some campaigns, as for the LAI in the eighth campaign. This scattering could be partly due to the uncertainties of the ground data estimates, as the satellite image displays similar values (around 6.5) for ground values ranging between 5 and 8. This is also explained by the well-known saturation of the signal for very high LAI.

As observed in the scatter-plots, a bias for bare areas is observed (dots over TF axis). This can be explained as the empirical function is adjusted for vegetated rice crops (dense vegetation in most campaigns). However, this should not introduce a significant bias in the mean values, as bare areas in the paddy rice area are very limited (just the narrow paths across the paddy fields).

6.3. THE HIGH RESOLUTION GROUND BASED MAPS

The ground estimated values were up-scaled using Landsat-8 imagery and empirical transfer function for 5 field campaigns where cloud-free images were available. The high resolution maps are obtained applying the selected transfer function to the Landsat-8 TOA reflectance. Figure 32 to Figure 35 present the TF biophysical variables over a 20x20km² area. Red square marks the 5x5km² study area. A mask have been applied to the water bodies (blue), it corresponds to the pixels where NDVI values are negative.

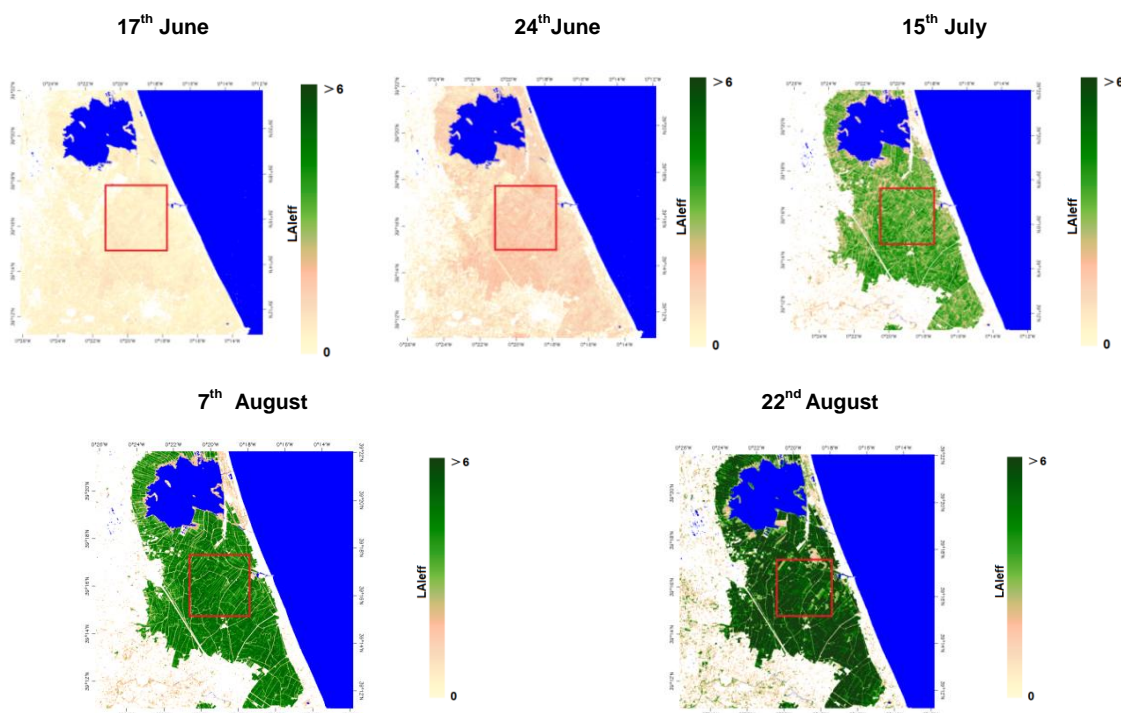


Figure 32: Ground-based LAleff maps (20x20 km²) retrieved on the Albufera Site for each campaign. Red square marks the 5x5 study area.

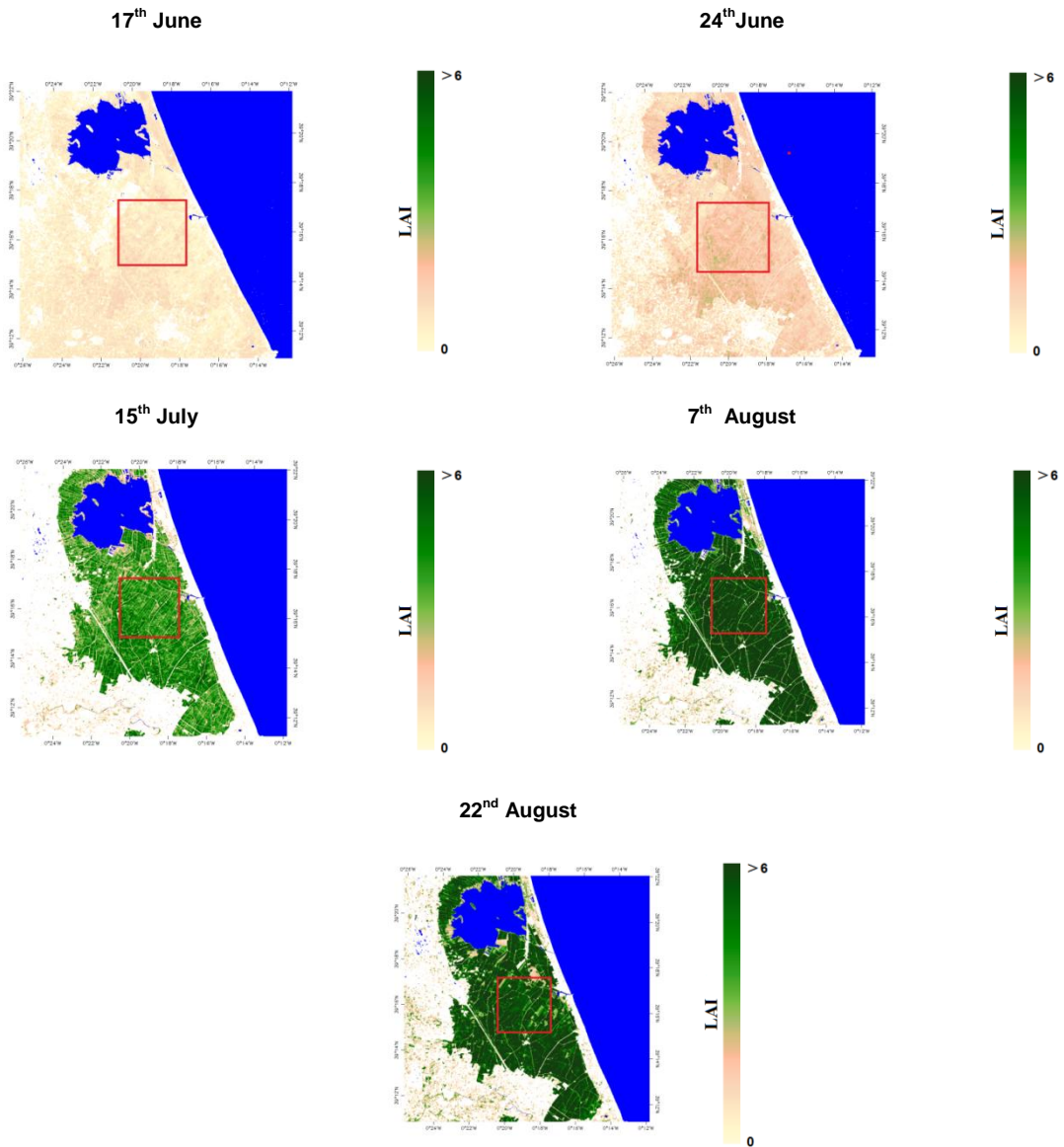


Figure 33: Ground-based LAI maps (20x20 km²) retrieved on the Albufera Site for each campaign. Red square marks the 5x5 study area.

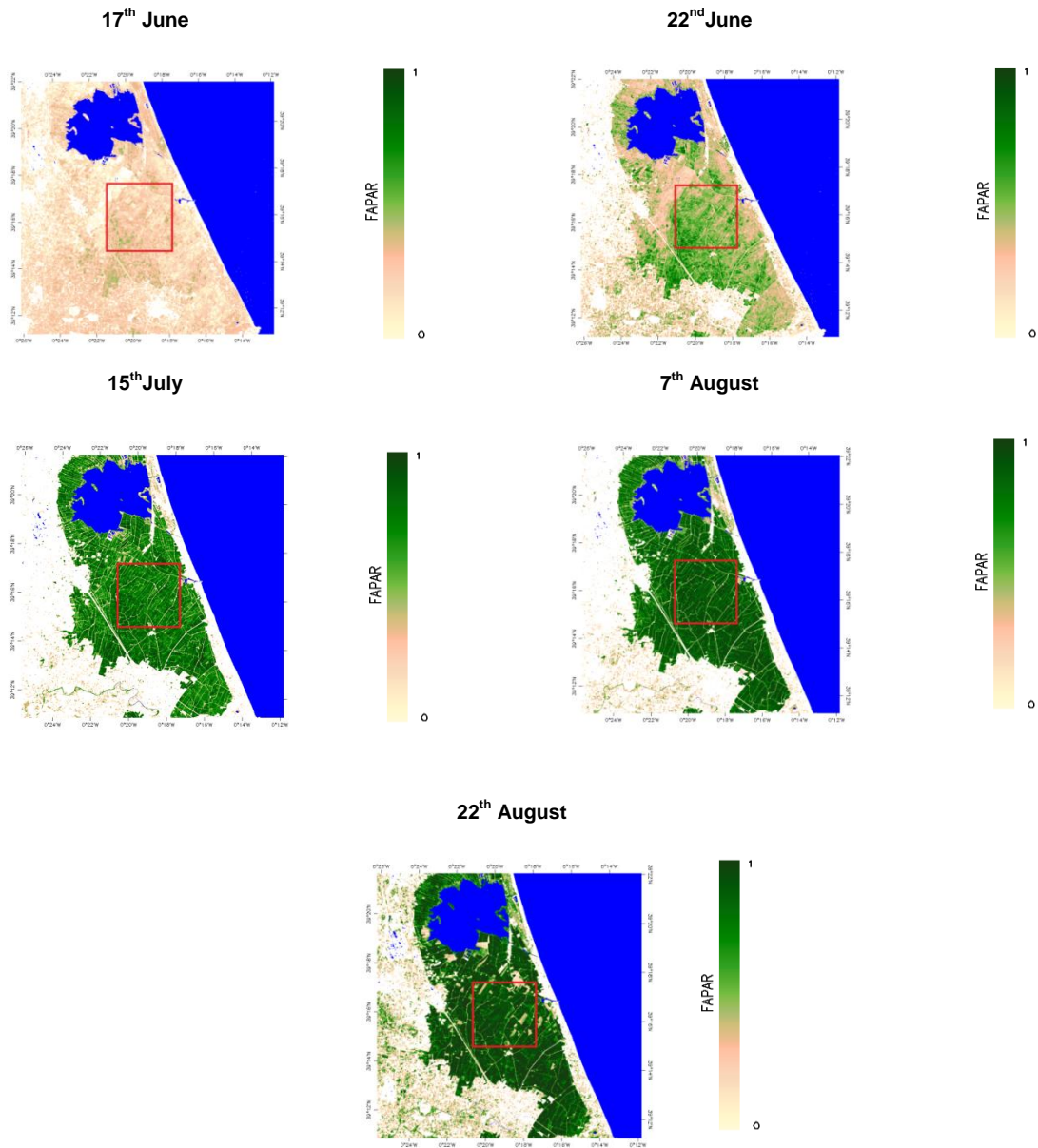


Figure 34: Ground-based FAPAR at 10:00 maps (20x20 km²) retrieved on the Albufera Site for each campaign. Red square marks the 5x5 study area.

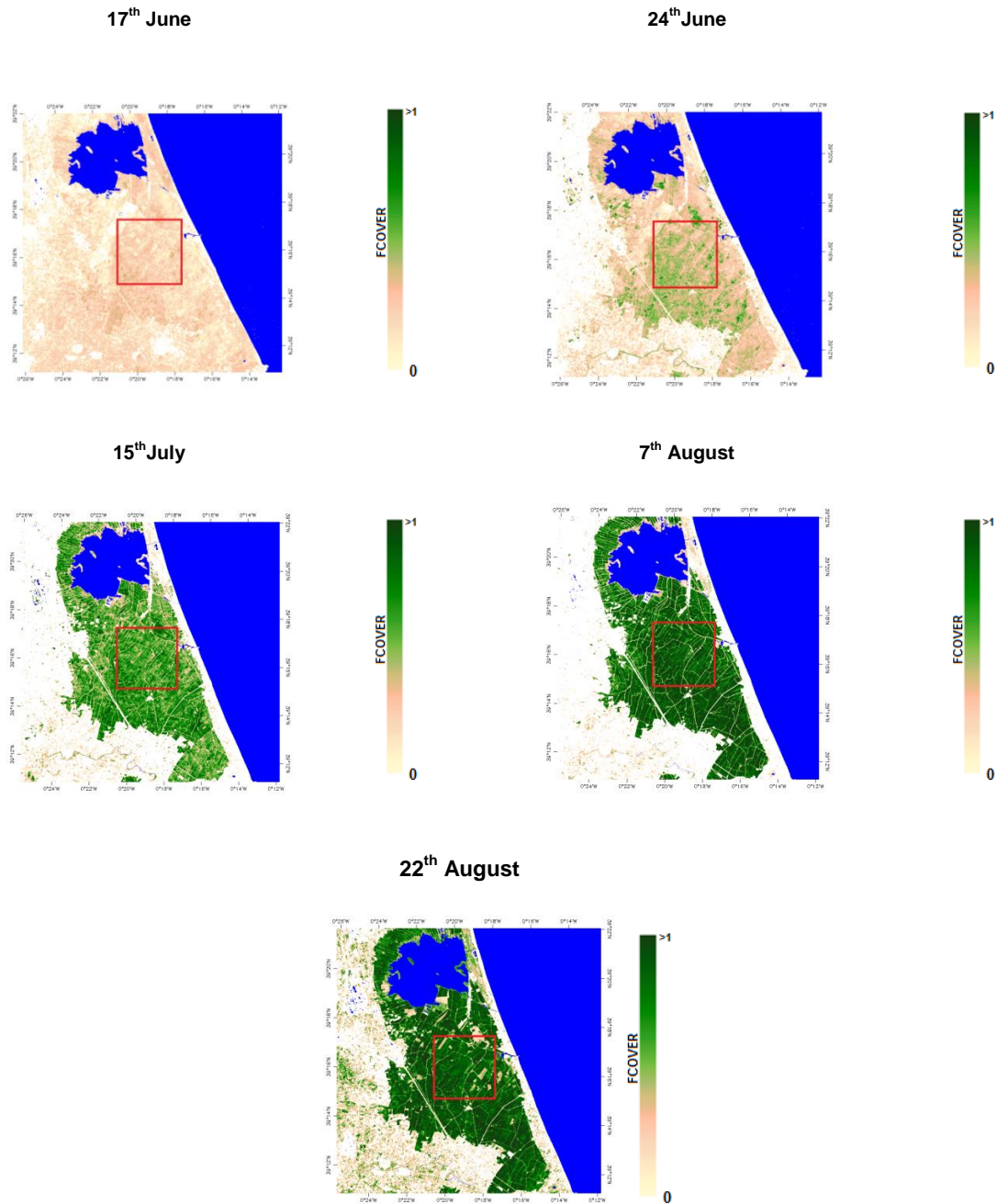


Figure 35: Ground-based FCover maps (20x20 km²) retrieved on the Albufera Site for each campaign. Red square marks the 5x5 study area.

6.3.1. Mean values for validation

Mean values of a 3x3 km² area centered in the test site are provided for validation of 1 km satellite products in agreement with the CEOS OLIVE direct dataset (Table 11). For the validation of coarser resolution products (e.g. MSG products) a larger area should be considered. For this reason empirical maps are provided at 5x5 km², and at 20x20 km². Table 11 summarizes the mean and standard deviation values of this 3x3

km² area for each campaign and each biophysical parameter. Note that the reported mean values for FCover should be considered with caution, as an underestimation of actual FCover is expected as explained in Section 4.3.

Table 11: Mean values and standard deviation (STD) of the HR biophysical maps for the selected 3x3 km² areas at Albufera site.

Campaign	LAI _{eff}		LAI		FAPAR		FCover	
	MEAN	STD	MEAN	STD	MEAN	STD	MEAN	STD
17 th June	0.45	0.18	0.58	0.27	0.21	0.08	0.18	0.07
24 th June	1.19	0.33	1.51	0.34	0.46	0.09	0.35	0.09
15 th July	3.16	0.72	3.76	0.83	0.73	0.14	0.59	0.14
7 th August	4.28	0.86	5.77	1.09	0.85	0.15	0.74	0.16
22 th August	4.57	0.92	5.90	1.28	0.85	0.20	0.80	0.19

Table 12 describes the content of the geo-biophysical maps in the "BIO_YYYYMMDD_SENSOR_Site ETF_Area" files, where

BIO stand for Biophysical (LAI_{eff}, LAI, FAPAR and FCover)

YYYYMMDD=Campaign date

Site = Albufera

ETF stands for Empirical Transfer Function

Area = window size 20x20 km² and 5x5 km²

Table 12: Content of the dataset.

Parameter	Dataset name	Range	Variable Type	Scale Factor	No Value
LAI effective	LAI _{eff}	[0, 7]	Integer	1000	-1
LAI	LAI	[0, 7]	Integer	1000	-1
FAPAR 10:00 a.m.	FAPAR	[0, 1]	Integer	10000	-1
Fraction of Vegetation Cover	FCover	[0, 1]	Integer	10000	-1
Quality Flag	QFlag	0,1,2 (*)	Integer	N/A	-1

(*) 0 means extrapolated value (low confidence), 1 strict interpolator (best confidence), 2 large interpolator (medium confidence)

7. CONCLUSIONS

The FP7 IMAGINES project continues the innovation and development activities to support the operations of the Copernicus Global Land service. One of the ImagineS demonstration sites is located at the "Albufera" site, close to Valencia (Spain), over rice crops in a wetland. This is one of the pilot sites of the FP7 ERMES project aimed to provide a downstream service over rice areas based on the assimilation of EO and in-situ data into a crop model.

This report first presents the ground data collected during a join multi-temporal field campaign with a total of 9 field campaigns conducted from June to August of 2014 by the University of Valencia (ERMES project) with the support of EOLAB (ImagineS). The dataset includes around 30 ESUs for each campaign. ESUs were characterized with different devices, including DHP, LICOR-LAI 2000 and LAI-2200, AccuPAR LP-80 and a mobile App (Pocket LAI). Digital hemispherical photographs were processed with the CAN-EYE software to provide LAI, LAI_{eff}, FAPAR and FCover, whereas AccuPAR provided FAPAR and LAI_{eff}, and LAI-2000, LAI-2200 and mobile App provided LAI_{eff} values.

An inter-comparison of the different devices was conducted over a few ESUs in three different campaigns for all the variables, whereas LAI_{eff} data was intercompared in the 9 campaigns. The results show a quite good agreement of the different estimates, with almost no systematic differences, except for the mobile App which systematically underestimate DHP or LAI-2000 measurements. The overall RMSE for LAI_{eff} is around 0.5 for the largest sampling, whereas discrepancies of LAI estimates (using two DHP) are around 1 LAI unit. For the FAPAR, the RMSE is slightly lower than 0.1, whereas for FCover is 0.11. Note that some discrepancies were found between the two DHP estimates, mainly for the campaign of August. The subjective criteria to classify green/soil elements, as well as the uncertainty in the classification due to the shaded vegetation elements explain the observed differences.

The DHP estimates of the FCover were found lower than expected for the densest vegetation stages. The underestimation of FCover was associated to the classification of shaded vegetation as soil. Thus, it is recommended to use with caution this information for validation.

Secondly, high resolution ground-based maps of the biophysical variables have been produced over the site. Ground-based maps have been derived using high resolution imagery (Landsat-8) according with the CEOS LPV recommendations for validation of low resolution satellite sensors. Transfer functions have been derived by multiple robust regressions between ESUs reflectance and the several biophysical variables. The spectral bands combination to minimize errors (weighted RMSE and cross-validation RMSE) were band 1 (green), band 2 (red) band 3 (Near Infrared) and band 4 (Short Wave Infrared) combination.

The quality flag map based on the convex-hull analysis shows very good quality around the center of the image (around 90% at 3x3 km² validation zone), with some

areas in the contours of the image, corresponding to water bodies or villages, where the level of confidence is lower.

The biophysical variable maps are available in geographic (UTM 30 North projection WGS-84 for first and second campaign and UTM 31 North projection, WGS 84 for the rest of campaigns.) coordinates at 30 m resolution. Mean values and standard deviation for LA_{eff}, LAI, FAPAR at 10:00 and FCover, were computed over the validation area of 3x3 km².

8. ACKNOWLEDGEMENTS

This work is supported by the FP7 IMAGINES project under Grant Agreement N°311766.

Thanks to the *Universitat de València* for the organization of the field campaign and for the ground data provided in the framework of FP7 ERMES project.

9. REFERENCES

Baret, F and Fernandes, R. (2012). Validation Concept. VALSE2-PR-014-INRA, 42 pp.

Camacho, F., Cernicharo, J., Lacaze, R., Baret, F., and Weiss, M. (2013). GEOV1: LAI, FAPAR Essential Climate Variables and FCover global time series capitalizing over existing products. Part 2: Validation and intercomparison with reference products. *Remote Sensing of Environment*, 137: 310-329.

Cabrera, A.L. (1976). Regiones Fitogeográficas Argentinas. En : W.F. Kugler (Ed.). Enciclopedia Argentina de Agricultura y Jardinería. Editorial ACME. Buenos Aires. Tomo 2 Fascículo 1.85 pp.

Canfalonieri et al. (2013). Development of an app for estimating leaf area index using a smartphone. Trueness and precision determination and comparison with other indirect methods.

Demarez, V., Duthoit, S., Baret, F., Weiss, M. and Dedieu, G. (2008). Estimation of leaf area and clumping indexes of crops with hemispherical photographs. *Agricultural and Forest Meteorology*. 148, 644-655.

Fang, H., W. Li, S. Wei, T. Sun, C. Jiang (2014a). Seasonal variation of leaf area index (LAI) over paddy rice fields in NE China: Intercomparison of destructive sampling, LAI-2200, digital hemispherical photography (DHP), and AccuPAR methods. *Agricultural and Forest Meteorology* 198–199 (2014) 126–141.

Fang, H., W. Li, S. Wei, T. Sun, C. Jiang (2014b). Paddy Rice Experiment in the Sanjiang Plain (PRESP). Field Measurements Report, 32pp.

Fernandes, R., Plummer, S., Nightingale, J., et al. (2014). Global Leaf Area Index Product Validation Good Practices. CEOS Working Group on Calibration and Validation - Land Product Validation Sub-Group. *Version 2.0: Public version made available on LPV website*.

LI-COR Inc., Lincoln, Nebraska, (2009). ftp://ftp.licor.com/perm/env/LAI-2200/Manual/LAI-2200_Manual.pdf

LI-COR Inc., Lincoln, Nebraska, (2013). http://envsupport.licor.com/docs/LAI-2200C_Instruction_Manual.pdf

Martínez, B., García-Haro, F. J., & Camacho, F. (2009). Derivation of high-resolution leaf area index maps in support of validation activities: Application to the cropland Barrax site. *Agricultural and Forest Meteorology*, 149, 130–145.

Miller, J.B. (1967). A formula for average foliage density. *Aust. J. Bot.*, 15:141-144

Morici, E. ; Muiño, W ; Ernst, R ; Poey, S. (2006). Efecto de la distancia a la aguada sobre la estructura del estrato herbáceo en matorrales de *Larrea* sp. Pastoreados por bovinos en zonas áridas de Argentina. *Archivos de Zootecnia*. Vol. 55. Nº 210. Universidad de Córdoba España. 149-159 p.

Morisette, J. T., Baret, F., Privette, J. L., Myneni, R. B., Nickeson, J. E., Garrigues, S., et al. (2006). Validation of global moderate-resolution LAI products: A framework proposed within the CEOS land product validation subgroup. *IEEE Transactions on Geoscience and Remote Sensing*, 44, 1804–1817.

Norman, J. M. and J.M. Welles., (1983). Radiative transfer in an array of canopies. *Agron. J.* 75:481-488.

Warren-Wilson, J., (1963). Estimation of foliage denseness and foliage angle by inclined point quadrats. *Austral. J. Bot.* 11, 95-105.

Weiss, M., Baret, F., Smith, G.J., Jonckheere, I. and Coppin, P., (2004). Review of methods for in situ leaf area index (LAI) determination. Part II. Estimation of LAI, errors and sampling. *Agricultural and Forest Meteorology*. 121, 37–53.

Weiss M. and Baret F. (2010). CAN-EYE V6.1 User Manual

Welles, J.M. and Norman, J.M., 1991. Instrument for indirect measurement of canopy architecture. *Agronomy J.*, 83(5): 818-825.